Development and Experimental Analysis of a Novel Hybrid Cooling Concept for Electric Vehicle Batteries

By

Yuyang Wei

A thesis submitted in Partial Fulfillment of the Requirements for the Degree of

Master of Applied Science

in

The Faculty of Engineering and Applied Science

Automotive Engineering

University of Ontario Institute of Technology

March 2018

Abstract

In this thesis, a novel hybrid cooling concept for electric batteries is developed and studied at both the cell-level and pack-level experiments. The concept is based on a simple air-cooling duct that utilizes enhanced water vaporization by convection to achieve an effective cooling. A series of hydrophilic fiber channels containing a water coolant is exposed to a forced air coolant to extract the latent heat from the battery. Air-cooling and water-cooling methods are also studied to compare and prove the cooling performance. From the test results, the hybrid cooling showed a much greater potential for battery packs with higher energy and power density. At the cell level, the contacted hybrid cooling method was able to decrease the highest temperature rise by 82.9%, 69.6%, and 57.3% compared to that of the no-cooling, the air-cooling, and the water-cooling tests, respectively; and the temperature decreased by 60.9% and 47.0% compared to the air- and water-cooling respectively for the contactless hybrid cooling. The maximum cell-level temperature non-uniformity by the contacted and contactless hybrid cooling tests are 4 ℃. and 2℃, respectively. At the pack level, the contactless hybrid cooling provided more than 70% improvement in both the cooling efficiency and the temperature uniformity compared to the no-cooling baseline.

Keywords: hybrid cooling, electric vehicle, lithium-ion battery, battery thermal management, cell-level, pack-level, air-cooling, liquid-cooling, phase-change material, evaporative cooling, experimental study.

Acknowledgements

I am truly thankful for my family's support, understanding, and love during all the time I study abroad alone in the past 6 years. My father as an engineer and my mother as a teacher, provide me important guides and assistance in my engineering study. I am also fortunate to have my girlfriend Youyou Sun taking care of my living and health, especially the hard period of my eye surgery during my graduate studies. Both my family and my girlfriend were the foundation of my support off-campus. I am also fortunate to have my friends Mohammed Ibrahim and Ahmad Hasan working in the same lab after our cooperation in undergraduate capstone project, and Mohammed's intelligence in CFD helped me a lot during the studies. My upperclassman and colleague Seham Shahid, who worked on a Li-ion battery air-cooling system before my enrollment, provided me uncountable assistances at the beginning of my research. Many thanks should also be given to my friends Kai Rasporich and David Capano from Electrical Engineering in UOIT, for guiding me while making the Li-ion battery pack for this thesis.

I am forever indebted to my advisor and mentor Dr. Martin Agelin-Chaab for his endless guidance and support since my undergraduate. His wisdom has provided me with insight that I will forever reflect upon. Financial support of this work by the Natural Sciences and Engineering Research Council of Canada is gratefully acknowledged.

Nomenclature

Alphabets

$A = surface\ area\ (m^2)$

$a_i = specific\ area\ (m^2)$

$C = correction\ coeficient\ constant$

$C_p = heat\ capacity\ \left(\frac{kJ}{kg \cdot K}\right)$

$D = diffusion\ cosfficient\ \left(\frac{m^2}{s}\right)$

$E_i = equlibrium\ potential\ (V)$

$F = Faraday\ constant\ (9.648456e + 04\ C/mol)$

$g = gravity\ acceleration\ \left(\frac{m}{s^2}\right)$

$h_a = enthalpy\ of\ air\ (J)$

$h_c = effective\ convective\ heat\ transfer\ coefficient\ \left(\frac{W}{m^2K}\right)$

$h_{vs} = enthalpy\ \ of\ water\ vapour\ at\ water\ surface\ temperature\ (J)$

$I = infiltration\ (m)$

$i = infiltration\ rate\ (\frac{m}{s})$

$I_i = current\ (A)$

i_i

$= current\ generation\ by\ a\ specific\ area\ of\ a\ layer\ of\ battery\ active\ material\ (A)$

$j_i = specific\ reaction\ flux\ (\frac{mol}{m^2 s})$

$k_{eff} =\ electrochemical\ reaction\ rate\ constant\ (\frac{m}{s})$

$k_T = effecitve\ thermal\ conductivity\ (\frac{W}{mK})$

$L = characteristic\ length\ (m)$

$m = mass\ (kg)$

$p = pressure\ (Pa)$

$Q = heat\ generation\ (W)$

$R = electric\ resisitance\ (ohm)$

$S = sorptivity\ (\frac{m}{s^{0.5}})$

$T = temperature\ (K)$

$t = time\ (s)$

$V = battery\ working\ voltage\ (V)$

$V_o = open\ circuit\ voltage\ (V)$

Greek symbols

$\beta = water\ evaporation\ \ mass\ transfer\ coefficient\ (\frac{kg}{m^2 Pa \cdot s}\ or\ \frac{kg}{m^2 s})$

$\eta_i = overpotential\ between\ adjacent\ anode\ and\ catode\ layers\ (V)$

$\mu = mean\ kinematic\ viscosity\ \left(\frac{m^2}{s}\right)$

$\rho = density\ \left(\frac{kg}{m^3}\right)$

$\sigma = electric\ conductivity\ (\frac{S}{m})$

$\varphi = moisture\ mass\ fraction\ \left(\frac{kg}{kg}\right)$

$\phi_s = electric\ potential\ (V)$

$\phi_e = electrolyte\ potential\ (V)$

Subscripts

$a = ambient\ air$

$b = battery$

$cc = connector\ contact$

$d = dry$

$eff = effective$

$i = integers, numbers$

$i, j = vector\ indexes\ in\ the\ transverse\ and\ longitudinal\ directions, respectively$

$ma = moisturized\ air$

$rad = radiation$

$SEI = solid\ electrolyte\ interface$

$s = saturated\ steam$

$surf = surface$

$w = water$

$wf = wet\ fiber$

Table of Contents

List of Tables

List of Figures

Chapter 1: Introduction

1.1 Background and motivation

Climate change and fossil fuel depletion are two topics that have generated a lot of passionate discussion in public discourse. Carbon dioxide (CO_2) emitted from fossil fuel combustion, which makes up 80% of the total greenhouse gas (GHG) emissions is considered the major reason for global warming (Florides et al., 2009; Li et al., 2013). Meanwhile, 17% of CO_2 emission was produced by road transportation alone in a report made in 2000 (Chapman, 2007), which could be listed as the third largest sector of CO_2 emission according to Figure 1.1. According to another report in 2002 (Chapman, 2007), 81% of the total transportation energy was produced by oil as shown in Figure 1.2, and this percentage kept growing because of the continuous increase in road transportations. Therefore, under the estimation of oil usage by Gilbert Masters (2008), oil resources are likely to run out within 30 years. The vehicle industry which is one of the largest fossil fuel consumers seeks alternatives to the traditional power resources for vehicles.

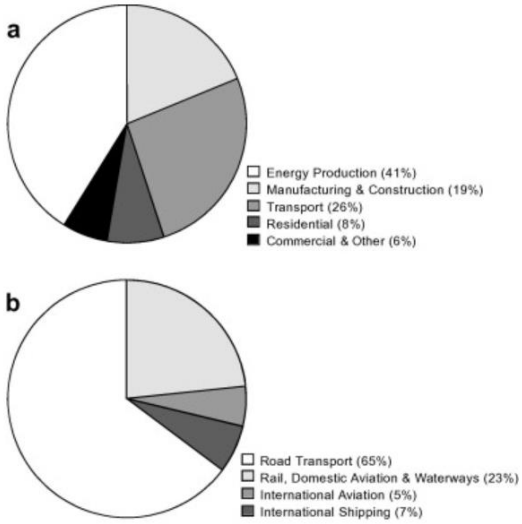

Figure 1.1: (a) Carbon dioxide emissions per industry/sector and (b) carbon dioxide emissions per the transport sector (Chapman, 2007).

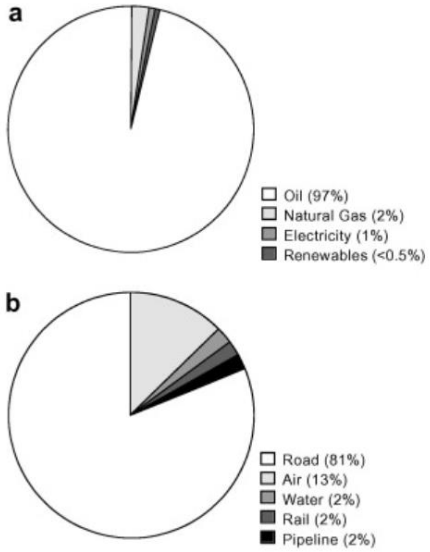

Figure 1.2: (a) Fuel use in the transportation sector in Organization for Economic Cooperation and Development (OECD) countries and (b) shares of transport modes in OECD countries (Chapman, 2007).

The two main power sources for road transportations under exploration that are also competing for the future energy market are hydrogen and electricity. Hydrogen has been well implemented in space transportation because it has the highest energy-to-mass ratio

among all the chemicals because it has the lightest molecular weight. It is also considered carbon-free, non-toxic, unlimited, and environmentally friendly. It produces only water after combustion with pure oxygen; however, due to its gaseous state in ambient and the limited availability in nature, technologies for mass production and storage are the two main barriers for wide application of hydrogen at present (Schlapbach, 2009). Toyota is still trying hard to push its hydrogen fuel cell vehicle (HFCV) Mirai into the larger market. Meanwhile, almost all the other manufacturers have started investing in electric vehicle (EV) technologies. Compared to hydrogen power, electricity has already been a major power source for our entire whole society, so it is easy to access. Storage of electricity for transportation applications can be easily achieved by using batteries. Although the energy-to-mass ratio of the best lithium-ion battery (LIB) car nowadays is still 50 times less than a gasoline car and it still needs a long time for charging (Kendall et al., 2017). The more mature technologies, flexibility in combination with present internal combustion engine (ICE) setups, and low carbon footprint still make the majority of manufacturers consider EV technologies as not only a transition but an alternative to the ICE with the most potential.

In fact, EV has been in the marketplace for decades as a so-called hybrid vehicle (HEV), but as Tesla brings its Model S into the competition, the public and national governments start turning eyes to the plug-in electric vehicle (PEV) which is driven by electricity purely. However, no matter the type of EV, battery technology is the key to the development and the market share of EVs. Among all kinds of battery chemistries, lithium-ion (Li-ion) is so far the best choice for EV energy unit design because of its high energy density, long cycle life, low self-discharge rate, and great efficiency compared to the others (Yang et al., 2015).

Meanwhile, performance and health of LIB are heavily related to its working temperature. One of the most popular EVs made by Nissan, the Nissan Leaf, was widely reported to have the problems of battery degradations in driving range and short battery pack lifespan in deserts and tropical regions because of poor cooling system design (Rahman et al., 2016). Therefore, battery thermal management (BTM) is critical to EV battery applications. The optimal working temperature for common LIBs is suggested between 25℃ to 40℃ (Rao et al., 2011; Jaguemont et al., 2016), and the temperature non-uniformity over the pack, calculated as the difference between the highest and the lowest cell temperature, should not exceed 5℃ (Shahid et al., 2017), however, the actual working temperature and non-uniformity can be much higher.

The charge and discharge current load on a rechargeable battery cell is measured as C-rate. 1C stands for a current rate reading that is same as the magnitude of the battery nominal capacity. For example, 1C charge rate for a 3.6 Ah Li-ion cell would be 3.6 A and 2C doubles it to 7.2 A. A high C-rate in both charge and discharge increases the load on the battery and hence the heat generation, which will be explained in more details in later chapters. For EVs, many situations such as racing, high loads on the air-conditioning system in hot summer days, and the newly developed fast charging technologies will require a charge or discharge current much higher than the 1C rate on the cells. This increases the thermal instability and hence battery degradation in the cell and pack levels, or even serious safety issues such as thermal runaway and cell explosion (Wang et al., 2012) as shown in Figure 1.3. Therefore, battery thermal management becomes one of the most critical barriers to the EV development. Different cooling methods are under aggressive research program in the field of EV battery thermal management, and they can be classified

into three directions: (1) air-cooling, (2) liquid cooling, and (3) phase-change material (PCM).

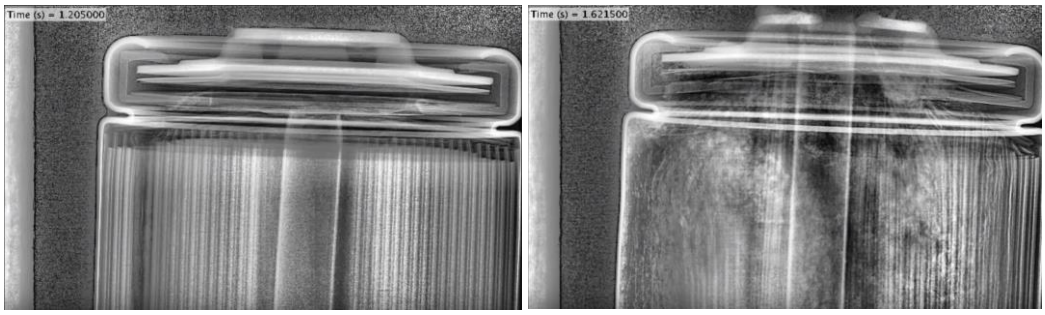

Figure 1.3: High-speed X-ray picture of a cylindrical LIB under normal (left) and thermal runaway (right) conditions (Finegan et al., 2018).

Air cooling is the most traditional cooling method. Air with relatively low thermal conductivity and heat capacity is not an ideal coolant for high heat components. However, as stated previously that the energy-to-mass ratio is important for the transportation sector, air cooling therefore is still popular in the field of research because of it is simple, passive, and light-weight design. Compared to the air cooling, cooling by liquids with much higher thermal conductivity and heat capacity is more popular with automobile manufacturers. Even though they are complex and heavy in design, which can affect the vehicle performance, the high cooling efficiency and controllability still make it stand out. Although PCM has been widely used in large-scale applications like thermal storage for buildings, its application in automotive industry is relatively new. PCM is becoming popular in this field because it combines advantages of the air cooling and the liquid cooling as it is a passive and simple system while it still comes with high cooling efficiency by extracting latent heat at melting. However, its total heat capacity is highly restricted by the mass of material, which potentially lowers the energy-to-mass ratio. Additionally, PCM

cannot be chilled by recirculation like in liquid cooling, so it is hard to control. There are also some studies investigating the use of heat pipes, however, heat pipes are expensive to be manufactured and are also heavy and complex. The pros and cons of the different cooling methods listed above indicate that given the right resources there is room for further improvement of the EV battery cooling system. New concepts can focus on a simple, light-weight, and energy saving design like the air cooling systems, a high cooling efficiency and controllability like the liquid cooling systems, and a passive as the PCM method. The system should also be user friendly and environmentally friendly so that the coolant can be released without causing harm to either human health or the environment.

1.2 Objectives

The primary research objective is to develop and experimentally verify a hybrid LIB thermal management system that has the capacity to maintain the temperature below 40 ℃ and temperature non-uniformity below 5 ℃. The proposed concept must be environmentally friendly and combine at least two different cooling methods directly onto the battery surface. The proposed system should work for both cell level and pack level. The detailed objectives listed below:

(1) Develop a thermal management concept for electric vehicles that employs at least two cooling effects by using two coolants.

(2) Develop a thermal management concept that is light-weight, simple, relatively passive, and environmentally friendly by using only nature fluids as coolants.

(3) Provide a proof of concept by building and setting up a laboratory model of the concept for cell-level and pack-level testing and experimentation.

(4) Provide insight and recommendations for further improvement based on the proof of concept results.

1.3 Thesis structure

This thesis is organized into six chapters including the current chapter. Chapter 2 highlights literature reviews for preparing this thesis, highlight the major contributions to the literature in the areas of LIB, EV battery cooling, and other heat exchanger applications. Chapter 3 introduces the methodologies including working principles, systematic design of the proposed system, test equipment, experiment setups and procedures, and error analysis. Chapter 4 analyzes and discusses the results. Chapter 5 summarizes the results and provides the conclusions of the study and recommendations for future work.

Chapter 2: Literature Review and Theoretical Background

In this chapter, electric vehicles (EVs) and batteries are introduced. Li-ion battery (LIB) categories and EV battery configurations will be briefly conducted. Different methods of EV battery thermal management are also reviewed in details. Above all, the background theories of the system working principle are presented.

2.1 Introduction to electric vehicles

There are different categories of EVs in the market for this transitional period from fossil fuel to sustainable power sources: hybrid electric vehicles (HEV), plug-in hybrid electric vehicles (PHEV), and plug-in electric vehicles (PEV).

HEVs can have multiple power sources onboard the vehicle. Usually, it is a combination of an internal combustion engine (ICE) and an electric motor (EM) power by a battery pack. HEVs use the ICE engine to charge the batteries. HEVs can be further categorized into series HEV and parallel HEV according to the complexity of control system. Series HEV generally couples an engine to a generator that is responsible for charging the battery, while the generator can also be used for extra propulsion power. In a parallel HEV, the ICE and the EM can work together or separately with a more complex control system. Various configurations can be seen in parallel HEV, depending on the roles of the engine and the electric motor. The engine size in a parallel HEV is generally smaller than that in a series HEV since the battery can take a larger share of power usage and hence parallel HEVs usually have a better fuel efficiency (Emadi et al., 2008).

PHEVs is a further improvement to the HEV. PHEVs have an externally-chargeable battery pack with high energy density and hence the electric power alone can provide a much longer mileage per charge, and hence a higher MPG rating (Emadi et al., 2008). Therefore, companies nowadays are putting more effort in developing PHEVs as the transition products because they are not only cleaner than conventional HEVs but also more user friendly. Meanwhile, the technologies in PHEVs are close to PEVs which will replace the former in future.

PEVs are entirely powered by electricity from a high energy density battery pack. Like PHEVs, they are charged externally. Configurations of PEVs can depend on the layouts of EM. PEVs are considered to have the lowest carbon footprint and most environmentally friendly if the electrical power source is not fossil fuels.

2.2 Electric batteries

There have been many types of batteries in use and the battery technologies have rapidly developed over the past decade because of the drive to achieve full transportation electrification. Energy density, the power density, the cycle life, calendar life, and the cost per kWh are the key factors that determine the quality of a battery (Mahmoudzadeh Andwari et al., 2017). For electric vehicles at present stage, the driving mileage and performance compared to the conventional ICE vehicles are the most critical concerns for the customers, and these are highly dependent on battery energy density and power density. Figure 2.1 shows the specific power (power density) versus specific energy (energy density) by different types of battery technologies in the market.

Batteries used in road vehicles are usually lead-acid type. As can be seen in Figure 2.1, the lead-acid battery can come with high specific power, but its specific energy is lower

than any other types of batteries except for the supercapacitor. That's why it needs to be consistently charged by a running ICE during driving or it will drain out of power quickly. It is good for conventional vehicles as the battery cannot be the only power source and lead-acid battery comes with the lowest cost per kWh among all the battery types in the figure.

Nickel Metal Hydride battery (Ni-MH) has been used in hybrid vehicles such as Toyota Prius. The Ni-MH battery technology is a mature technology that has reached its best potential, both in cost reduction and characteristics (Mahmoudzadeh Andwari et al., 2017). It works fine with hybrid vehicles as its specific power and specific energy are high enough to take a part of the driving power, but not for PEVs in which the battery can be the only power source.

Among all the other battery types, it is found that Li-ion battery (LIB) usually can provide a relatively high performance in both specific power and specific energy, due to the fact that lithium possesses both the highest electrochemical potential and a low elemental mass (Mahmoudzadeh et al., 2017). Therefore LIB is considered the most promising for the EVs in the near future. Even though it comes with the highest cost per kWh and presents safety issues, the technology still has room for development.

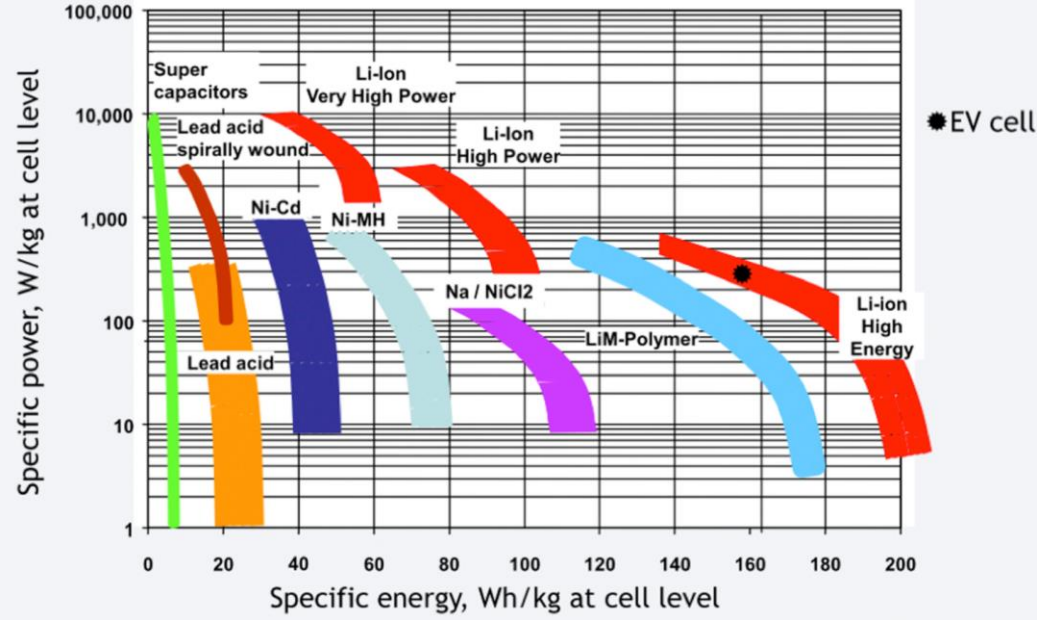

Figure 2.1: Specific energy and power of the common battery technologies (Mahmoudzadeh et al., 2017).

2.2.1 Lithium-ion batteries in electric vehicles

There are different kinds of Li-ion battery chemistries. LIB can be classified by battery chemistry and geometry. $LiCoO_2$ (LCO), $LiMn_2O_4$ (LMO), and $LiFePO_4$ (LFP) are the three most common categories. The LCO generally has a relatively high energy density, but short in power density, lifespan, and thermal stability (Zhao et al., 2011; Julien et al., 2014).The LMO, with a lower internal resistance because of the spinel manganese cathode structure, generally has better thermal stability, and hence works better with fast charging and discharging. However, compared to the LCO, the LMO lifespan is shorter and the energy density is lower (Shan et al., 2013). The LFP batteries generally have the highest scores in lifespan, power density, and thermal stability among the three, but have low energy density (Julien et al., 2014). New battery materials and technologies are being explored as the Li-ion market share is growing quickly.

There are basically three types of LIB geometries used in EVs: cylindrical, prismatic, and pouch (elliptic) cells. No matter which geometry is used, EV battery packs are constructed at three levels: cell, module, and pack level (Rao et al., 2011). Figure 2.2 demonstrates the LIB geometries commonly used in EVs and how the battery pack is constructed.

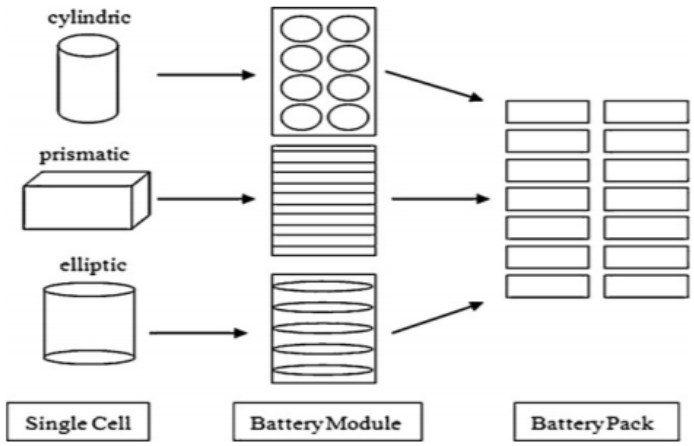

Figure 2.2: Geometries of LIB cells commonly used in EVs and demonstration of packaging layouts (Rao et al., 2011).

Tesla, Nissan, and Chevrolet have introduced their EVs into mass production for years, and their battery geometries are different. Tesla uses over 7000 cylindrical cells in its Model S, while Nissan Leaf and Chevrolet Volt use prismatic and pouch cells, respectively. With the huge success made by Tesla's Model S, the 18650 cylindrical Li-ion batteries used in their products might be the most famous among the three. According to the established data from the U. S. Environmental Protection Agency and U.S. Department of Energy (2015), the Tesla Model S a range of 539 km on a single charge, while the competitors were around 100 to 200 km (2014-2015 Nissan Leaf ranges around 135 to 172 km, and the 2016 Chevrolet Volt ranges around 85 km). Despite there are differences in

battery chemistries and thermal management system design, a higher energy density of cylindrical Li-ion battery compared to the prismatic cells used in Nissan Leaf and the pouch cells in Chevrolet Volt might also contribute to the longer driving range (Drake et al., 2014). Cost efficiency is another advantage of the cylindrical cells. Mass production can be achieved more easily and quickly for the cylindrical cells (Messina, 2015). Additionally, increasing the dimension of the battery cell can further lower the cost per unit power production (Ciez, and Whitacre, 2017). Tesla stated a 50% increment in cylindrical battery dimensions would contribute to a larger volume and hence 200% increment in energy density, therefore, the 21700 cylindrical cells might be used in Tesla future products. Therefore, one can conclude that a further increase in cell dimensions would contribute to a higher energy density.

However, heat accumulation in cylindrical cells is more obvious than the other battery geometries. Because layers of the functional chemicals and separators are rolled as a cylinder, as shown in the Figure 2.3, the central layers heat dissipation hardly benefits from any surface cooling effect (Drake et al., 2014). The cylindrical geometry also makes it hard for uniform cooling, which will be discussed in the following subsection in more details.

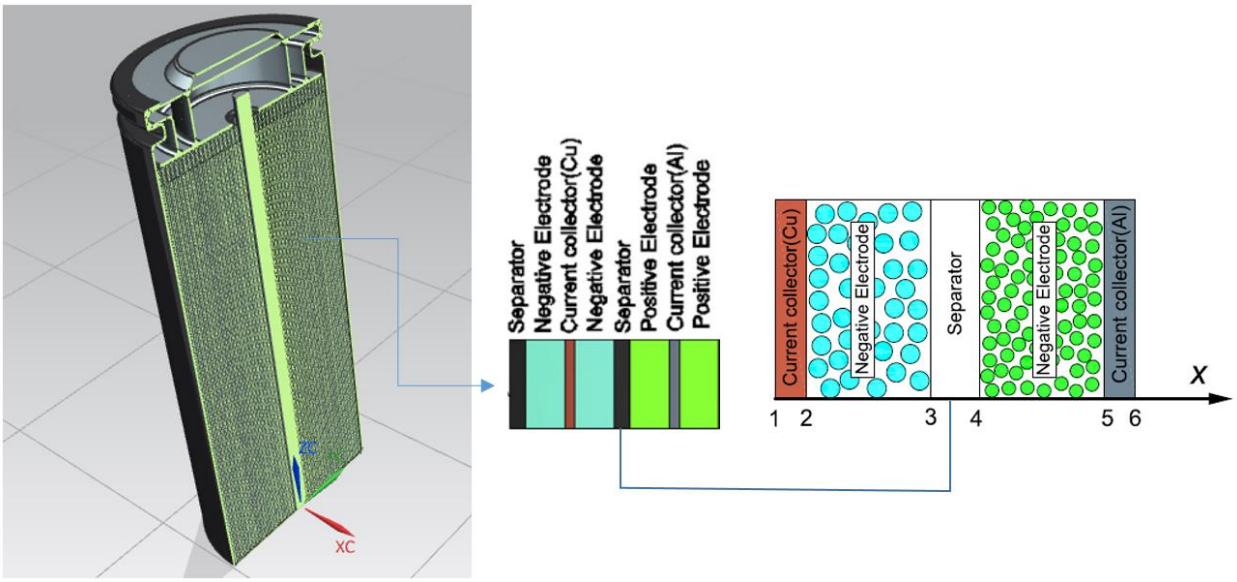

Figure 2.3: Illustration of the rolling multi-layer structure of a cylindrical Li-ion battery cell and the electrochemical model for each layer (Yang et al., 2015).

2.2.2 Methods for thermal management

As mentioned above, the charge and discharge current load on a rechargeable battery cell is measured as C-rate. A high C-rate in both charge and discharge increases the load on the battery and hence the thermal instability (Wang et al., 2012). Therefore, battery thermal management is critical for EV applications. Three cooling methods have been widely studied in the field of EV battery thermal management: (1) air-cooling, (2) liquid cooling, and (3) phase-change material (PCM).

Air-cooling is the most traditional cooling method in the industry. It is still very popular because of the advantages of its simple structure, low energy consumption, lightweight, low cost of development and maintenance, and environmental friendliness (Rao et al., 2011). However, the low thermal conductivity and heat capacity of air does not make it an ideal coolant. The air-cooling efficiency is highly dependent on the ambient

temperature. Additionally, prediction of the airflow behaviors within a battery pack can be difficult. Both Yang et al. (2015) and Tong et al. (2016) studied the effect of in-line and staggered layouts on a simplest cylindrical battery pack under unidirectional air cooling. Yang et al. (2015) simulated the cooling performance for both a single cell and a pack consisting of 26650 Li-ion batteries using the symmetric plane method by assuming the flow pattern is symmetric to the center line of the cells (Liu et al., 2015), as shown in Figure 2.4. The optimal pack design was judged to be the in-line layout with pitch distances of 34 mm transversely and 32 mm longitudinally. Ironically, Yang et al. (2015) suggested that the in-line layout performed better than the staggered one, while Tong et al. (2016) stated the opposite. The difference may be due to the different size of batteries used by the researchers (Yang et al. used 26650 cells while Tong et al. used 18650 cells). From the contrasting conclusions of Yang et al. (2015) and Tong et al. (2016), one can conclude that the design criteria for the air-cooling systems for different battery sizes and pack dimensions may not be consistent. From Figure 2.4, it is also found that the temperature at the cell leeward is higher than the other regions, because of flow wake regions developed there, recirculating and hence cumulating heat generated from the cells.

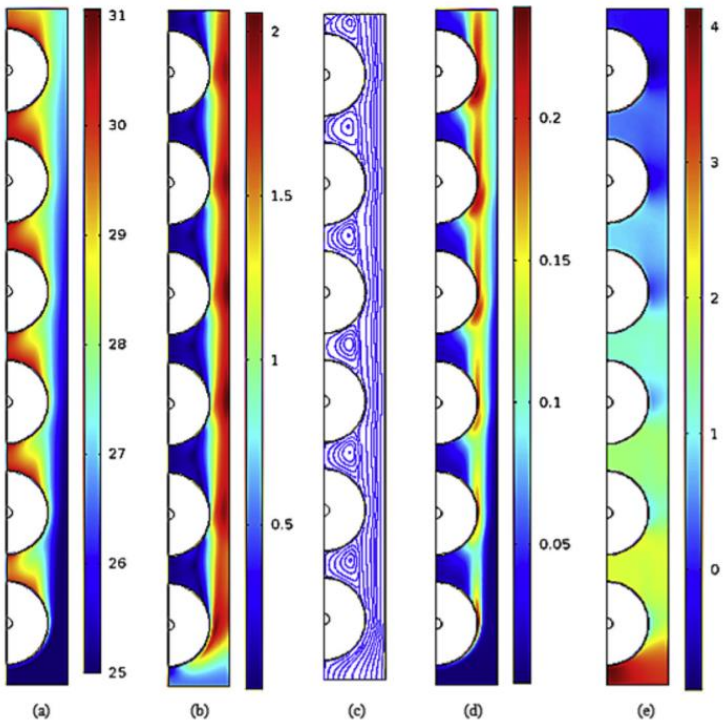

Figure 2.4: Simulated distribution contours at the end of discharge for the aligned battery pack with S_y = 34 mm: (a) temperature (℃), (b) velocity (m/s), (c) streamline, (d) turbulent kinetic energy (m^2/s^2) and (e) pressure (Pa) (Yang et al., 2015).

In order to eliminate the heat accumulation by this leeward effect on cylindrical cells in a unidirectional air cooling designed as Figure 2.5(a), Park (2013) designed and investigated prismatic battery pack with converging inlet and diverging outlet air ducts for more uniform airflow distribution along the pack, and simulated the effect of a pressure release vent, as shown in Figure 2.5(b). Saw et al. (2016) and Sun et al. (2014) simulated Park's idea (2013) on a cylindrical 38120 Li-ion battery pack. Liu et al. (2014) designed a nested air-cooling system by applying the same idea to not only the pack level but also each battery module inside the pack, as shown in Figure 2.6. Even though these duct designs had improved the cooling efficiency and the uniformity, their packs are geometrically asymmetric by the converging inlet and diverging outlet duct designs. Hence,

they may be hard to assembly in EVs as battery modules. With the complex external and internal duct designs, the energy density of the design from Liu et al. (2014) was highly restricted by the large cell-to-cell gaps. All these factors make it hard to employ their designs in commercial vehicles.

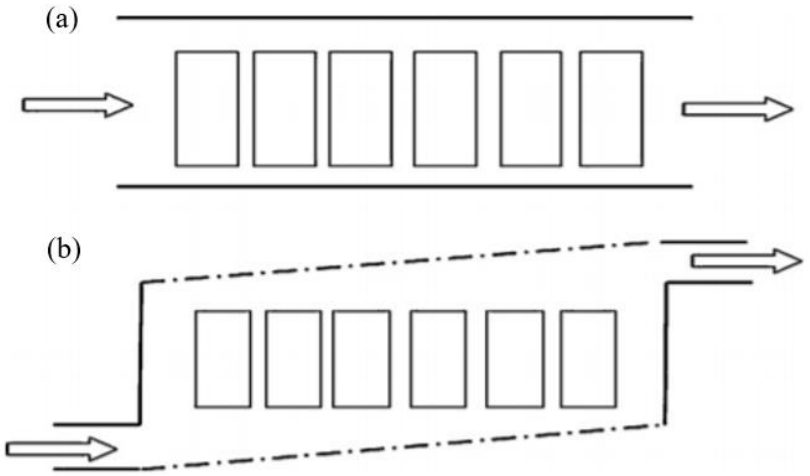

Figure 2.5: Air cooling system designed with (a) unidirectional flow with identical inlet and outlet, and (b) distributed vertical flow with converging inlet and diverging outlet (Rao et al., 2011).

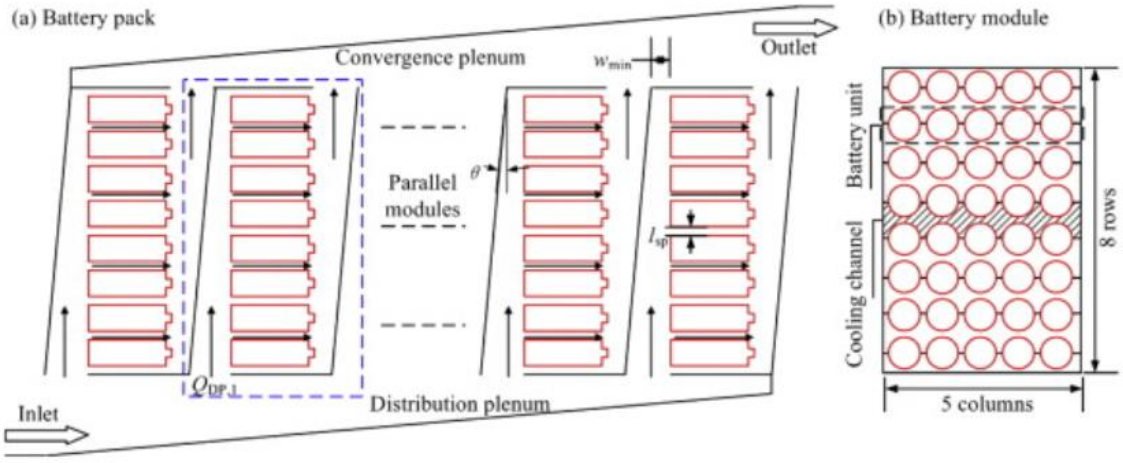

Figure 2.6: (a) The schematic of a nested air-cooling system in a battery pack. Arrows indicate the airflow directions. (b) The arrangement of battery cells in a battery module (Liu et al., 2014).

As mentioned earlier, for the cylindrical battery pack, unidirectional airflow is not effective in cooling because of the wake regions at the leeward side of the cells, and the heat cumulates from the pack inlet to the outlet. This leads to a faster degradation of cells around the outlet region than the inlet because of the long-term temperature non-uniformity. Additional studies investigated active air-cooling systems with reciprocating flows for uniformity improvement (Ling et al., 2015; Fan et al., 2013; Sasmito et al., 2012; Mahamud et al., 2011; Tong et al., 2016). However, the reciprocating flow concept could not improve cooling efficiency much because the properties and the flow pattern of air do not change by the reciprocation. The process only helped improve the temperature uniformity, as shown in Figure 2.7. Tong et al. (2016) suggested that the temperature uniformity can be positively correlated with the reciprocating frequency of the airflow. However, the high frequencies of reciprocating flow are expensive to implement and decrease system reliability dramatically. Most of the studies above showed that the air-cooling method can work properly under low battery discharge rates. However, it was noted that the air-cooling method alone is not effective enough for higher discharge rates (Park, 2013; Saw et al., 2016; Sun et al., 2014; Liu et al., 2014).

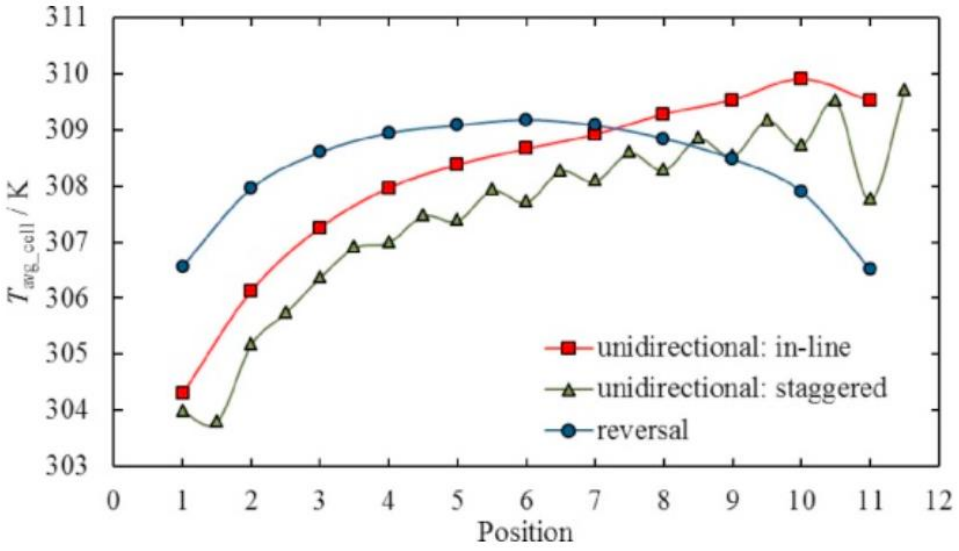

Figure 2.7: Instantaneous average temperature of cells at different positions (1 to 8: from the inlet) under unidirectional and reciprocating (reversal) flows (Tong et al., 2016).

Liquids usually have much higher thermal conductivity and heat capacity than air which makes liquid-cooling generally more effective; however, liquid-cooling needs circulation systems including pumps, pipings, and well-designed flowrate control systems (Rao et al., 2011). This makes it complicated in structure and system design, heavyweight, costly and consume more energy. Some existing liquid cooling methods employ glycol or water as the coolant, however, different coolant material could be used. Pouch or prismatic cells were used more often than the cylindrical cells in this research field since they allow simpler and compact structure of cooling plates shown in Figure 2.8 (Panchal et al., 2015, 2017). Lan et al. (2016) and Xu et al. (2017) simulated a design of aluminum mini-channel water cooling system for a prismatic cell and examined the effect by the number of coolant flow channels and the mass flow rate. The optimized design helps remain a working temperature lower than 27.8 ℃ and a maximum non-uniformity across a prismatic cell surface as 0.8 ℃ under 1C discharging rate. Similarly, Zhao et al. (2015) designed a mini-

channel liquid cooling system for a pack consisting of large size 42110 cylindrical batteries. The system was reported to handle a maximum temperature below 40 ℃ but failed to remain a non-uniformity lower than the limit of 5℃. Additionally, the water flow rates for these studies are high (0.2 L/min (Lan et al., 2016) and 0.06L/min (Zhao et al., 2015)), so an active recirculation system is required. The coolant flow rate for normal EV battery pack can be even much higher as about 10 L/min (He et al., 2017; Xu et al., 2017).

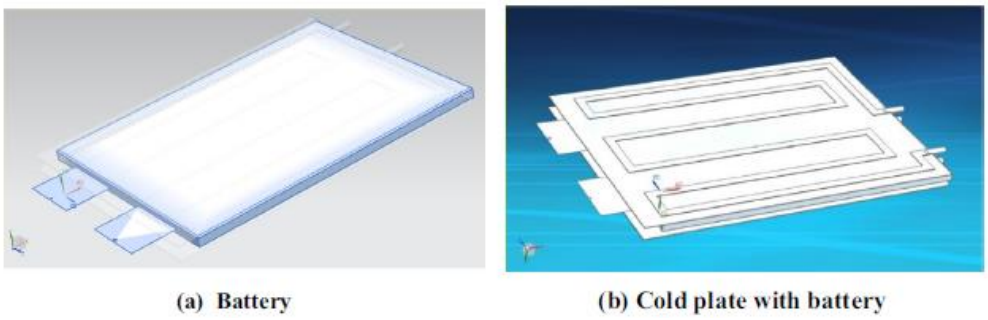

(a) Battery (b) Cold plate with battery

Figure 2.8: A liquid cooling plate design for a pouch battery (Panchal et al., 2015, 2017).

PCM has been widely studied for thermal storage in large-scale applications such as building energy conservation and climate control (Cao et al., 2017). However, PCM as a thermal management system is relatively new to battery applications. Essentially, a PCM cooling system is a purely passive. With the ability to trap latent heat while melting, PCMs theoretically have the highest cooling efficiency (Rao et al., 2011). Cooling can be achieved by simply dipping the whole heat source into PCM, hence PCM cooling comes with the best uniformity. However, PCM can also be heavy and not environmentally friendly. Additionally, the material of PCM usually cost much more than those used in the other cooling methods. Kizilel et al. (2009) compared the cooling efficiencies between PCM and the force air-cooling method under abusive conditions using simulations. It was

shown that PCM was superior in cooling performance and could prevent thermal runaway. However, Ling et al. (2015) argued that the heat taken out by PCM also needs to be extracted by other cooling methods because the total heat capacity of a certain amount of PCM is limited. Hence, Ling et al. (2015) and Fathabadi (2014) developed the so-called the “hybrid” cooling system that used the air-cooling to absorb the excessive heat from a PCM pack. Furthermore, PCM can inversely function as a secondary coolant to cool down another coolant. El-Ladan et al. (2015) presented an evaporative fan pad thermal management system design. The system uses fans to force the air (primary coolant) to flow across an evaporative pad before getting into the battery pack. The water (secondary coolant) is supplied to the pad and vaporizes inside, cooling down the air trapped from the ambient. Another PCM-like cooling approach is the heat pipe. Shah et al. (2016) built a mini heat pipe inside a cylindrical battery cell. However, heat pipes usually contain complex inner structures and special chemicals with low boiling points, making it too expensive for industrial applications.

2.2.3 Summary of the literature

For all the studies mentioned above, it following can be concluded. (1) The air-cooling method is usually simple in structure, light-weight, energy-saving, but has the worst cooling efficiency and uniformity. Improvement in cooling performance could sacrifice the simplicity and the battery pack energy density. (2) The liquid cooling method has higher efficiency and better uniformity, but need a circulation systems which adds complexity, weight, and energy consumption. (3) The PCM method can provide the best cooling performance both in terms of the temperature rise and uniformity, however, since the thermal capacity is dependent on mass, PCM systems are usually heavy or require

additional cooling systems to extract the heat from the PCM pack. (4) Coolants chosen for the liquid cooling and the PCM systems may not be environmentally friendly. Even though Ling et al. (2015) and Fathabadi (2014) mentioned the idea of a hybrid cooling system that combines different cooling methods, the batteries within their designs are only cooled by PCM, while the air coolant was used to cool the PCM. Hence, their methods can only be seen as an improvement of the PCM based cooling systems. The above factors provide the motivation for the present work, which proposes a hybrid EV battery cooling concept that combines at least two cooling methods directly.

2.3 Theoretical Background

This section will explain how the proposed concept can achieve a better cooling performance than the other cooling methods reviewed in the previous sections. Theoretical explanation will be firstly made by equations from battery heat generation. The energy governing equations for different models of hybrid cooling design are given after. Above all, the relation between the flow rates by the capillary pressure and the vaporization is discussed theoretically in the end.

2.3.1 Battery heat generation

The heat generation for Li-ion batteries comes from polarization, reversible heat by the chemical reactions, connector resistance, and internal resistances (Saw et al., 2013; Yang et al., 2015; Smith et al., 2006). The equations for these heat sources are complex as the internal resistances include electronic conductive resistance (resistance of active materials in positive and negative electrodes, and current collector), ion conductive resistance (electrolyte resistance), and the resistance from the solid electrolyte interface

(SEI) film on the negative electrode (Yang et al., 2015). Therefore, the general thermal equation of heat conduction within a lumped battery model can be expressed as (Saw et al., 2013; Yang et al., 2015; Smith et al., 2006):

$$\rho C_p \frac{\partial T}{\partial t} = \nabla \cdot k_T \nabla T + Q_p + Q_{rea} + Q_c + Q_{ohm} \tag{2.1}$$

Where k_T is the effective thermal conductivity of the active battery materials, $Q_p, Q_{rea}, Q_c, Q_{ohm}$ are heat generation from polarization, reversible heat by chemical reactions, electric contacts, and internal resistance, respectively:

$$Q_p = a_i j_i F \eta_i \tag{2.2}$$

$$Q_{rea} = a_i j_i F T \frac{dE_i}{dT} \tag{2.3}$$

$$Q_c = \frac{\left(I_i^2 \frac{R_{cc}}{A_{cc}}\right)}{Vol} \tag{2.4}$$

$$Q_{ohm} = \sigma_{eff,i} \left(\frac{\partial \phi_{s,i}}{\partial x}\right)^2 + k_{eff,i} \left(\frac{\partial \phi_{e,i}}{\partial x}\right)^2 + \frac{2k_{eff,i} RT(1-t_+)}{F}\left(1 + \frac{dlnf_\pm}{dlnc_i}\right)\frac{\partial lnc_i}{\partial x}\frac{\partial \phi_{e,i}}{\partial x} + a_i j_i F \Delta\phi_{SEI} \tag{2.5}$$

a_i is the specific surface area, j_i is the specific reaction flux, F is the Faraday constant $(9.648456e+04\ C/mol)$. The product of these three parameters is the current i_i produced by the specific area a_i:

$$i_i = a_i j_i F \tag{2.6}$$

However, a simplified and commonly used equation for the heat generation was given as (Abudul-Quadir et al., 2014; Liu et al., 2014):

$$Q_{total} = I_i(V_o - V) - I_i T \frac{dV_o}{dT} \tag{2.7}$$

Where Q is the heat generation in the battery cell, V_o is the open circuit voltage, V is the cell working voltage, I_i is the applied current and T is the temperature of the cell. The first term on the right-hand-side of the equation is essentially an integral form of Equation

2.2, but it stands for the irreversible heat generation by the overpotential of the whole circuit, which concludes all the heat generation by polarization and internal resistance. The second term is actually the integration of Equation 2.3 and stands for the reversible entropic heat generation by the total chemical reaction within a cell (Abudul-Quadir et al., 2014; Liu et al., 2014).

2.3.2 Water evaporation

The mass flow rate of water evaporation for a unit area ($kg\ s^{-1}\ m^{-2}$) can be calculated as:

$$\dot{m}_{wev} = \beta(p_s - p_a) \tag{2.8}$$

Where β is the convective mass transfer coefficient, and it is related to the airflow velocity; p_s and p_a are the saturated steam partial pressure at water temperature and the vapor partial pressure at the ambient air temperature. However, it was argued that the water evaporation rate is nearly impossible to be predicted due to its complex and stochastic nature (Turza et al., 2017).

Equation 2.8 can also be written in the form of the humidity ratio φ as (Turza et al., 2017; Leroux et al., 2015):

$$\dot{m}_{wev} = \beta(\varphi_s - \varphi_a) \tag{2.9}$$

Where the transfer coefficient β is hard to predict as stated above, but the equation for the coefficient is given by the Sherwood criterion (Sh) (Turza et al., 2017):

$$Sh = \frac{\beta L}{D\ H^{\frac{1}{4}}} = C.(Re)^a.(Ar)^b.(Sc)^d \tag{2.10}$$

Where *Re*, *Ar*, and *Sc* are the Reynolds, Archimedes, and Schmidt numbers, respectively.

2.3.3 Energy governing equations

In the proposed hybrid cooling method, a combination of convective heat transfer by air, and latent heat trapped by vaporized water are employed. As the fiber channel makes no contact with the battery surface, energy governing equations similar to El-Ladan et al.'s model (2015) can be used:

$$m_b c_{p_b} \frac{dT}{dt} = Q_g - Q_{mar} \tag{2.11}$$

$$Q_{mar} = h_c A_b (T_b - T_{ma}) \tag{2.12}$$

Where ($m_b c_{p_b} \frac{dT}{dt}$) denotes the energy change respect to time of a battery cell, $\mathrm{Q_{mar}}$ is the heat removed by moisturized air convection.

The airflow will be cooled before hitting the battery surface by the wetted fiber channels. The heat taken out from the air by the water is provided by the equation in El-Ladan et al.'s study (2015):

$$m_a \, dh_a = [h_c(T_a - T_w) + \beta(\varphi_s - \varphi_a)h_{vs}]dA \tag{2.13}$$

Where m_a is the mass of airflow, A is the surface area of the fiber channels exposing to the airflow.

From Equation 2.9, it can be concluded that lower relative humidity can contribute to a higher water vaporization rate, which can trap larger amount of latent heat. Additionally, it is pointed out that a lower humidity decreases water droplet temperature (Fuijta et al., 2010), and hence further increase the convective cooling effect according to Equation 2.13. However, it should be pointed out that the convective heat transfer coefficient h_c would not be affected by the relative humidity since the Nusselt number (Nu), shown in Equation 2.14, was experimentally proved not to change with the relative humidity (Fujita et al., 2010; Bread et al., 1971).

$$Nu = \frac{h_c L}{k_T} \tag{2.14}$$

In a variation of the proposed concept, the fiber channel can make direct contact with the battery surface. Therefore, Leroux et al.'s energy model (2015) shown in Figure 2.9 could be used.

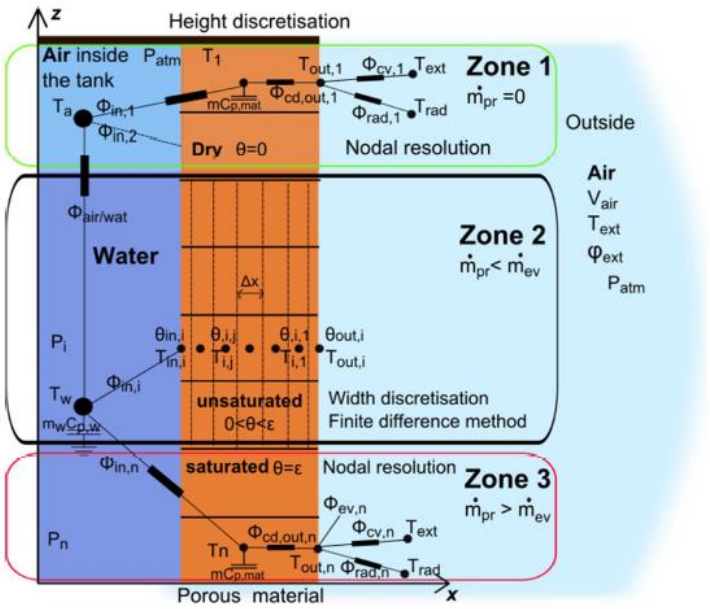

Figure 2.9: Leroux et al.'s model (2015) of a porous wall for building an evaporative cooling system.

From Figure 2.9, three different situations of Leroux et al.'s porous cooling wall (2015) are analyzed: (1) drywall, (2) partially wetted wall, and (3) saturated wetted wall. The three situation will also be applicable to the fiber channel in this proposed design. However, since the thickness of the fiber channels e are much thinner than Leroux's porous cooling wall, the moisture gradient in the heat conduction orientation would be neglected in this study. This makes the following equations good enough to describe all the three situations:

$$m_b c_{p_b} \frac{dT}{dt} = Q_g - h_c A_{ex}(T_b - T_{ma}) - \int k_{wf} \frac{\partial T}{\partial n} dA_{wf} \tag{2.15}$$

Where k_{wf} the effective conductive heat transfer coefficient for the wetted fiber channels is, n denotes the distance in the heat conduction orientation, A_{ex} and A_{wf} are the battery areas exposed to the air and covered by the wet fiber, respectively.

According to Leroux et al. (2015), the heat conducted into the fiber channels will be transferred to the ambient by convection, radiation, and vaporization:

$$k_{wf}\frac{\partial T}{\partial n} = e\rho_{wf}c_{p_{wf}}\frac{\partial T}{\partial t} + h_c\left(T_f - T_a\right) + h_{vs}\beta(p_s - p_a) + \epsilon_{surf}\sigma(T_f^4 - T_{rad}^4) \quad (2.16)$$

Where $\left(e\rho_{wf}c_{p_{wf}}\frac{\partial T}{\partial t}\right)$ the energy per unit area causing the temperature change in the wetted fiber channel, L is the latent heat of evaporation, h_m is the evaporative mass transfer coefficient, ϵ_{surf} is the emissivity on the fiber channel surface.

2.3.4 Capillary action within fiber channels

The water coolant was purely driven by the capillary effect. The flow rate of the liquid within a fiber material can be simply expressed by taking derivatives of the cumulative infiltration I (i.e. the distance the liquid travel through the fiber material) over a short time t (Philip, 1957):

$$I = S\sqrt{t} \quad (2.17)$$

Therefore:

$$\frac{dI}{dt} = i = \frac{0.5S}{\sqrt{t}} \quad (2.18)$$

Where S is the so-called sorptivity. The equations above are good for horizontal infiltration where the capillary effect is the only force acting on the liquid. For vertical or angled infiltration where gravity is significant, a parameter A_1 can be added to Equation 2.17. The estimation of capillary flowrate within fibers can be more complex if evaporation

of the liquid is accounted for in the calculation. From the equations above, we can see that the infiltration rate by the capillary effect decreases non-linearly over time.

The capillary pressure is defined as the difference in the phase pressures:

$$p_c = p_n - p_w \tag{2.19}$$

Where P_n and P_w are the pressures of non-wetting and wetting phases, respectively. Therefore, it is known that the capillary infiltration rate can decrease to 0, with the fiber moisture saturation increasing to 1(Iliev et al., 2013). Hence, if the liquid vaporization rate cannot go over the infiltration rate at one fiber region with the highest capillary pressure, the coolant mass flow rate within the fiber can be determined by the vaporization rate instead of the capillary effect, similar to the Zone 2 shown in Figure 2.9 (Leroux et al., 2015):

$$\dot{m}_{cap} = \dot{m}_{ev} - \dot{m}_{pr} \tag{2.20}$$

Where $\dot{m}_{cap}$, $\dot{m}_{ev}$, and $\dot{m}_{pr}$ are the mass flow rate by capillary pressure, evaporation, and hydrostatic pressure, and the hydrostatic pressure can be zero if the fiber locates over the liquid free surface.

Chapter 3: Methodology

In this chapter, the systematic outline of the proposed method is presented. The experiment setups, procedure, and error analysis will be reported. Additionally, the equations for a theoretical explanation of the working principles of the proposed designs are discussed.

3.1 Design description of the proposed concept

The design of the proposed system is based on a simple air-cooling duct in which there are series of hydrophilic fiber channels, which can be exposed to the airflow to extract the latent heat from the battery. A water coolant is driven through the fiber channels purely by capillary forces. Therefore, the system can utilize enhanced water vaporization by air convection to achieve an effective cooling. Figure 3.1 demonstrates two design variations of the proposed concept being tested in this study.

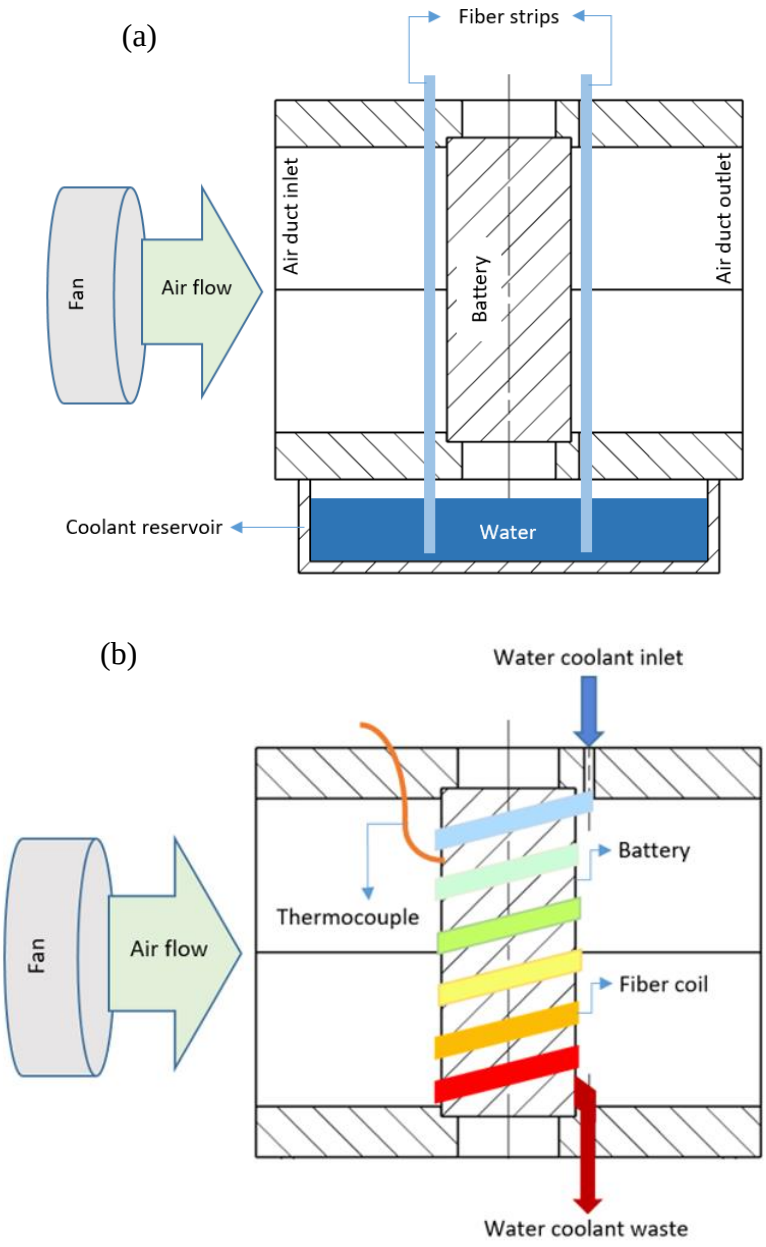

Figure 3.1: Schematic of the proposed hybrid cooling concept designed with (a) fiber channel making no contact with the cell surface, and (b) fiber channel coiled around the cell surface and directly in contact.

The proposed design is applicable to any type of battery (cylindrical, prismatic, or pouch type in different sizes or dimensions) or electric energy supply that requires cooling.

A battery mount forms a duct with an inlet and an outlet, allowing convective coolant to flow through. The hydrophilic or super-hydrophilic fiber material is also positioned and retained by this mount. The fiber can be either in contacted or not in contact with the battery surface, serving as fiber channels for the conductive and evaporative water coolant. For the case with the fiber channels in contact with the battery surface, a super-hydrophilic fiber material with high thermal conductivity is preferred. The energy unit mounts in this study has the air flow duct placed horizontally as shown in Figure 2.5(a), so that the air will flow perpendicularly to the center line of the energy unit. In a variation of the design, multiple air ducts can be placed vertically as shown as Figure 2.5(b), so that the air can flow parallel to the battery center line and a better flow uniformity can be achieved. The reservoir for the water coolant continuously provides water coolant to the fiber channels. The reservoir is located under the energy or battery packs so that the water is driven by capillary effect only. This also naturally constrain the water from running off the fiber due to the surface tension between water and the fiber. Additionally, after the fiber strips are saturated wet, the water flow rate will be purely controlled by the rate of water vaporization. This eliminates the requirement of a flow rate control system.

Figure 3.2 shows the schematic overview of one possible system configuration. Three cooling stages can be designed, for example, a pure air-cooling mode can be assigned as first-stage cooling intended for the small-load driving mode, a second-stage water-cooling is suitable for a further temperature control in a medium-load driving mode, and a final-stage hybrid cooling mode is able to cool down the batteries in an extreme-load driving mode. Condensation from the air-conditioner (A/C) can be recycled as the water coolant. The low-temperature condensate from the A/C can enhance the cooling efficiency. A low-

power pump might be required only for transporting the A/C condensate to the reservoir, while the working fluid (or water) in the cooling system is driven purely by capillary effect, with no extra power required from the batteries. The water coolant can be specifically applied to locations with the most heat accumulation for optimal pack-level uniformity. The air and the water coolant can be released to the ambient after use without harming the environment since no toxic chemicals are involved.

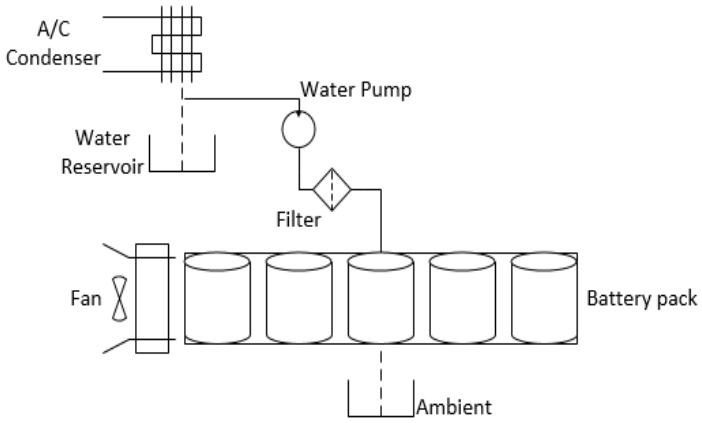

Figure 3.2: A conceptual system configuration of the proposed hybrid cooling system.

3.2 Experimental materials and equipment

Tests were designed to compare the cooling performance among air-cooling only, water-cooling only, and the hybrid cooling with different under different conditions. The 26650 IMR LIB with a capacity of 5200mAh from ShenZhen Fest Technology Co. with the specifications shown in Table 1 was used as the battery in each experiment. This battery was chosen because of its high capacity and high allowable draining load so that a discharging time long enough for building up the heat could be obtained under a relatively

high C-rate. A small model wind tunnel with an outlet size that matches the battery pack inlet was custom made with an axial fan. All the experiments were conducted at room temperature of around 21 ℃. The inlet air velocity for the air-cooling and the hybrid cooling test are set to around 0.7 m/s by the anemometer, which is consistent with the study by Yang et al. (2015).

A 4-channel multifunctional battery charger/discharger (Reaktor Quadcore $4 \times 300\ W\ 20A$) was used only for charging a single battery at a time in all the cell-level tests. Its draining power was too low to discharge over 1C. Therefore, a multifunctional load (TDI RBL488) which can go up to 120 A or 800 W high-power draining load was used for discharging. For all the pack level tests, eight battery cells connected in series are charged and discharged at the same time. Therefore, balance charging was required. Since the multifunctional charger/discharger can only do balance charging for a pack with a maximum of 6 cells, it is hence replaced by a power supply connected with a battery management system (BMS) circuit board suitable for 8S connection (8 batteries in series). The TDI RBL488 electric load is still responsible for discharging in the pack level tests. The battery, charger, and the discharger are connected in parallel as the discharger could also be used as a multimeter to monitor different working parameters of the battery.

The thermal behaviors of the batteries were measured by both an infrared thermal camera (SPI IRXP-5000, specifications shown in Table 2), a K-type thermocouple built inside an Omega HFS-4 thin film heat flux sensor (specifications shown in Table 3), and a T-type thermocouple (specifications shown in Table 4). The infrared camera was used specifically for temperature uniformity observation; the thin-film heat flux sensor with a K-type thermocouple was used to collect the original data for battery heat generation in the

no-cooling case; the T-type thermocouple with small sensor tip was used to measure the surface temperature for a smaller area. The infrared images from the thermal camera are recorded by a screen recorder. The thermocouples are connected to a data acquisition board (National Instrument cDAQ-9188XT), which was integrated with the LabVIEW software for data logging and analysis. A multifunction anemometer (Proster TL107) with temperature range from -10 to 40 ℃ was used to measure ambient temperatures. The accuracy of the anemometer reading was within ± 0.1℃. A weight scale (OHAUS PA153 with the specifications in Table 5) was used to measure the mass flow rate of the water coolant and water vaporization rate.

The infrared thermal camera has two modes of temperature measurement: spot (Sp) and areal (Ar). The spot mode only reads the temperature at the assigned pixel location, while the areal mode automatically calculates a temperature by averaging all the pixel-wise temperature readings within a defined area as shown in Equation 3.1 (Tanda, G., 2015):

$$T_{Ar_{avg}} = \frac{\sum_{i=1}^{n}(T_{Ar_i} A_{Ar_i})}{\sum_{i=1}^{n} A_{Ar_i}} \tag{3.1}$$

Where T_{Ar_i} and A_{Ar_i} are pixel-wise temperature and area, respectively, and n stands for the total number of pixels within the defined area. The areal mode can also automatically sense the highest and the lowest local temperatures for the defined area. The accuracy of the areal mode is hence higher than using the spot mode when it measures the overall temperature over a surface. Therefore, the areal mode should be preferred wherever it is possible.

For the water cooling and the contacted hybrid cooling tests using gravity as the main driving force for the liquid water coolant flow. Carbon fiber tows with excellent longitudinal thermal conductivity are chosen for the fiber channel coils. For the contactless

and contacted hybrid cooling test using capillary pressure as the only driving force for the liquid water coolant flow, paper towels were chosen as the fiber channel material after testing the infiltration rate of several simple materials such as candle wick and carbon fiber. The carbon fiber channels were used in the water-cooling and the contacted hybrid cooling tests only. The carbon fiber tows are weaved like braids, as shown in Figure 3.3 (a). This increases the sectional size of the fiber channel and hence the coolant flow rate. Paper towel material used in the contactless hybrid cooling tests are twisted into channels as shown in Figure 3.3 (b). For the water cooling and the hybrid cooling tests, the water temperature was maintained around 20 ℃. The gravity-driven water flow rate at the inlet of carbon fiber channel is determined to be about 0.015 to 0.020 g/s. A water flow rate higher than this value can cause water running off the fiber channel. For the contactless hybrid cooling using capillary-driven flow, the water flow rate is purely dependent on the evaporation flow rate, which has been discussed in the previous section of theoretical background.

Figure 3.3: (a) Weaved carbon fiber tow used in water-cooling and contacted hybrid cooling tests; (b) twisted paper fiber strip used in the contactless hybrid cooling test.

Table 1. Battery Specifications (ShenZhen Fest Technology Co., ltd., 2017; Lygte-info.dk., 2018)

Properties	Specifications
Supplier	Efest
Chemistry	$LiMn_2O_4$ (IMR/LMO)
Diameter	26.5±0.2 mm
Height	65.98±0.2 mm
Weight	92±1 g
Nominal capacity	5200 mAh
Nominal voltage	3.7 V
Charge cut-off voltage (overvoltage limit)	4.1±0.1 V
Discharge cut-off voltage (undervoltage limit)	2.5±0.1 V
Maximum continuous discharge current	15 A
Maximum pulse discharge current	40 A
Calculated internal resistance	0.15 ohm

Table 2. Thermal Camera Specifications (SPI Corporation, 2018)

Properties	Specification
Detector type	FPA, uncooled ASi Microbolometer
Thermal resolution	384 x 288 / 640 x 512 pixels and 1024 x768 XGA HD
Spectral range	8 – 14 µm
Field of view	17.5 x 13 degrees
Thermal sensitivity	≤ 80 mk @ f/1.60 Hz, 300 K
Temperature range	-20 – 100 ℃
Accuracy	± 2% of reading
Measurement mode	Spot (Sp), area (Ar), isotherm, profile, auto hot spot, auto alarm
Emissivity correction	Variable from 0.01 to 0.99 in 0.01 increments
Measurement features	All correction based on distance, relative humidity, atmospheric transmission & external optics

Table 3. Thin Film Heat Flux Sensor Specifications (OMEGA Engineering inc., 2018)

Properties	Specification
Model	Omega HFS-4
Temperature limit (℃)	-200 ~ 150
Nominal sensitivity ($\frac{\mu V}{Btu/Ft^2 \cdot Hr}$)	6.5
Max recordable heat flux (Btu/Ft^2Hr)	30,000
Built-in thermocouple	Type K
Thermal capacitance ($Btu/Ft^2°F$)	0.02
Thermal resistance ($°F/Btu/Ft^2Hr$)	0.01
Nominal thickness (mm)	0.18

Table 4. Accuracy for Typical Type-T Thermocouples (National Instruments Corporation, 2017)

Measuring temperature (in degrees Celsius)	Maximum tolerance allowance (in degrees Celsius)
-200	3.0
-100	1.5
0	0.5
200	0.8

Table 5. Weight Scale Specifications (Ohaus Corporation, 2018)

Properties	Specifications
Equipment name	OHAUS Pioneer PA153
Maximum capacity	150 g
Readability	1 mg
Linearity	$\pm$0.002 g
Repeatability (typical)	0.001 g
Stabilization Time	2 seconds

3.3 Experimental setup and procedure

3.3.1 Cell-level setup and temperature measurement

For cell-level tests, the battery after each test run was replaced with a brand new identical battery to avoid the effect of battery degradation. Instead of using a spot welder with nickel strip for the electrode connector, which make it impossible to disassemble once welded, copper wires with high electric conductivity and low electric resistance are coiled as the external electrode connectors. This allows quick swap between old and new batteries. The battery pack was made by the 3D printer for fast modeling and assembly. Figure 3.4 and Figure 3.5 show the schematics of the setups and the photographs of the equipment used in the cell-level tests.

The case of no cooling was made as the baseline. Figure 3.6 (a) shows the experimental setup for the cell-level no-cooling baseline. The heat flux sensor is responsible to measure the heat generation rate over the battery cell surface. The camera faces to the leeward side of the battery cell, and an areal measurement Ar1 is assigned to the cell surface to locate

the highest local temperature and verify the average temperature presented by the heat flux sensor. For all the tests using liquid coolant channels, since the channels cover a part of the battery surface, the spot mode of infrared measurements is precisely assigned to different locations of the battery surface as shown in Figure 3.6 (b) and (c), so that the readings of the battery surface temperature are not affected by the channel temperature. For example, in the cell-level water-cooling and the contacted hybrid cooling tests, the transverse temperature changes were measured at 3 spots at the top (Sp1, Sp2, and Sp3) and 3 spots at the bottom (Sp5, Sp6, and Sp7). Additionally, in order to keep the consistency of measurement, the same setup is also used in the air- cooling case even though there is no fiber channel used in the test. The axial temperature changes were measured at Sp2, Sp4, and Sp6. An extra areal infrared temperature measurement was placed at Ar1 in Figure 3.6 (b). It measured the average temperature at the location where the T-type thermocouple is attached.

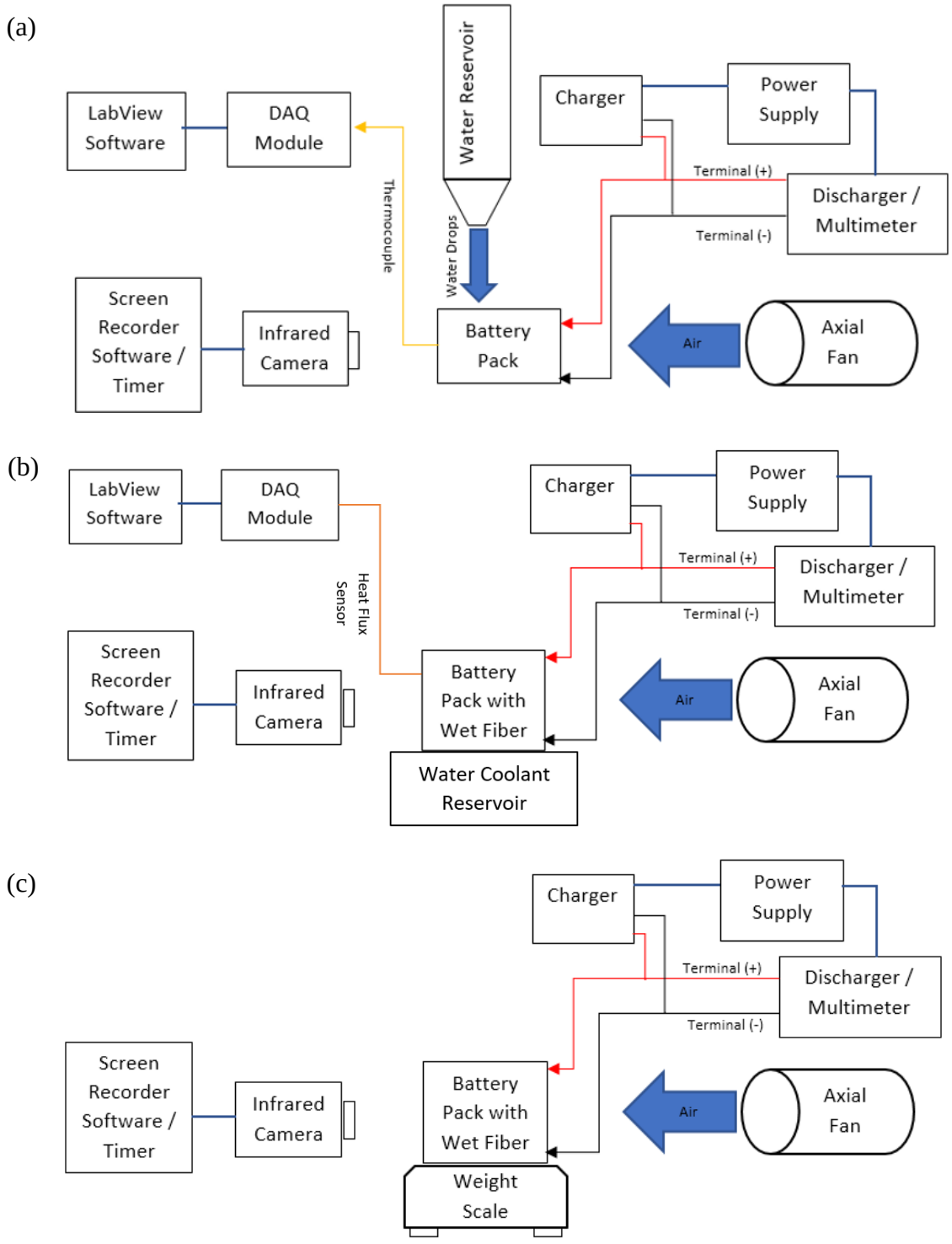

Figure 3.4: Schematics of experimental setups:(a) temperature rise and uniformity measurements for water only and hybrid cooling using gravity to drive the liquid coolant, (b) temperature rise and uniformity measurements for hybrid cooling using capillary effect to drive the liquid coolant, and (c) water vaporization mass flow rate measurement.

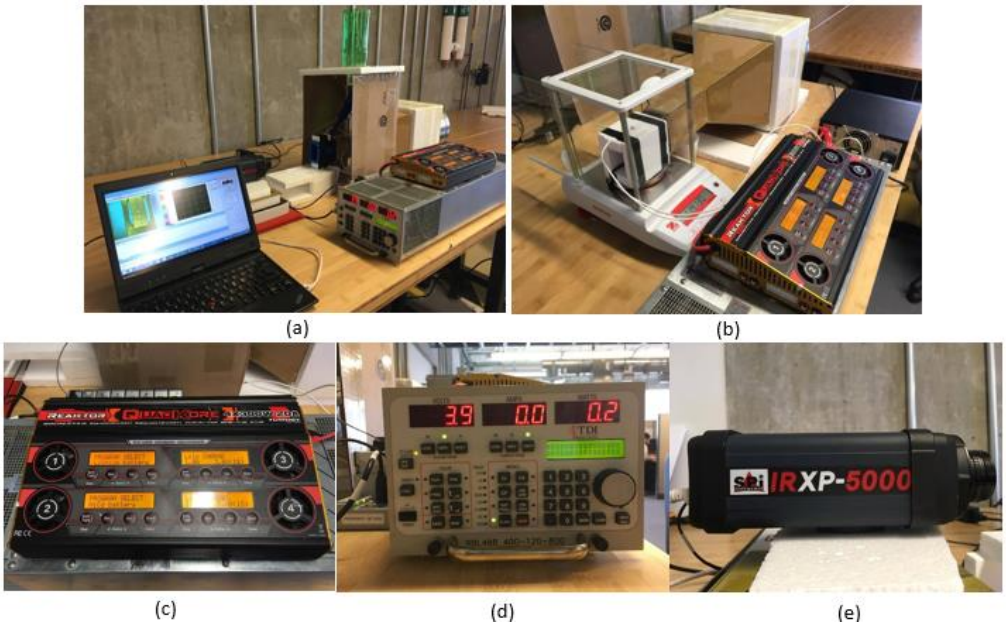

Figure 3.5: (a) Experimental setup for: (a) temperature measurements; and (b) water evaporation rate measurement. (c) Li-ion battery charger; (d) Li-ion battery discharger; (e) infrared thermal camera.

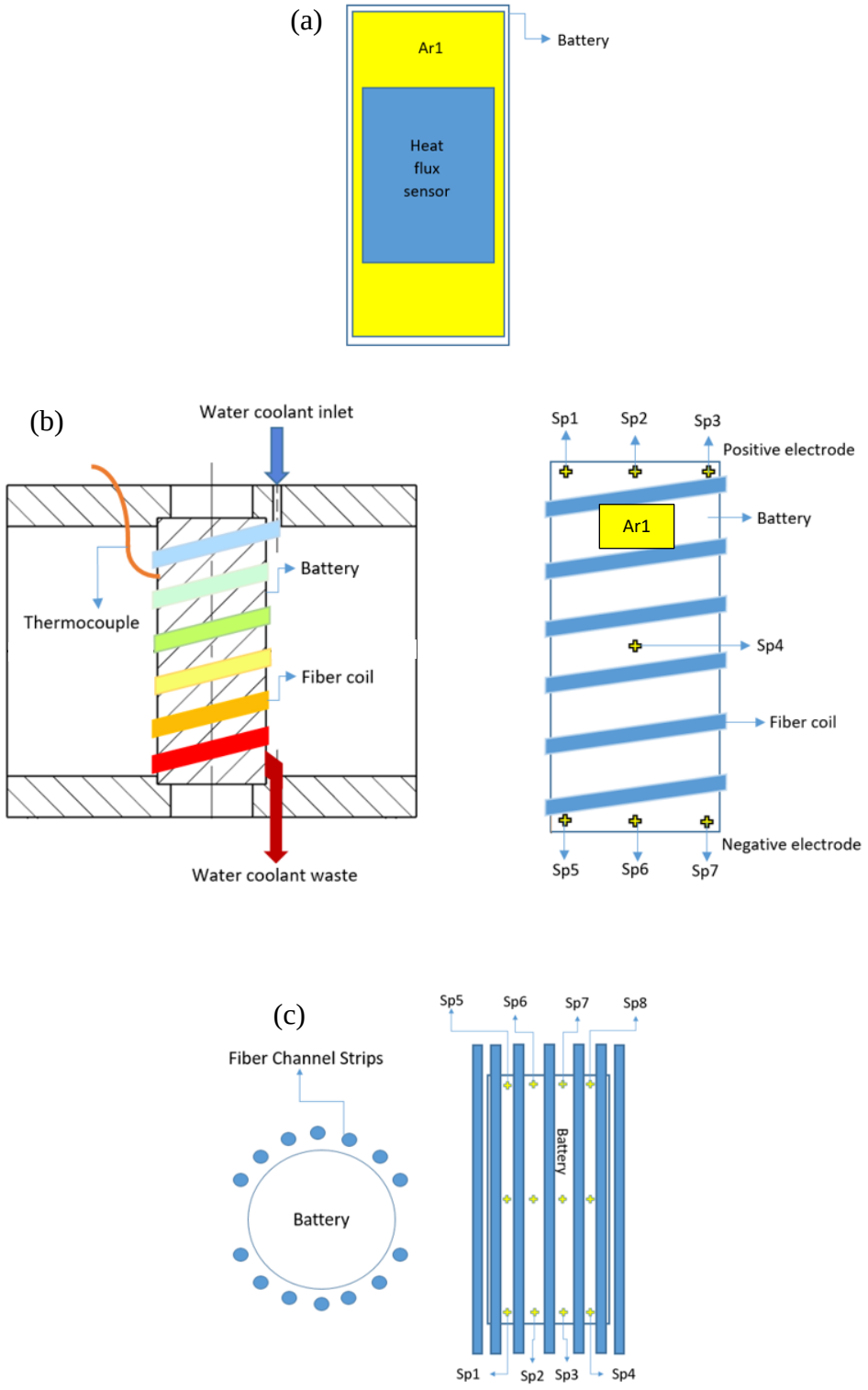

Figure 3.6: Infrared measurement and thermocouple setup for cell-level tests: (a) no cooling and air cooling, (b) water cooling and contacted hybrid cooling, and (c) contactless hybrid cooling.

For all the cell-level temperature measurements, the batteries were charged to 4.0 V using constant current and constant voltage (CC-CV) method with charging currents starting at 1.0 A (< 0.2 C). The charging processes were cut off when the charging current dropped to 0.1 A (≅ 0.02 C). By maintaining a low charging current, the battery temperatures were stable at around 26℃, hence no significant degradation occurred during the charging period. The batteries were further chilled down to room temperature (21 ℃) after charging to ensure electrochemical equilibrium. The discharger measured the voltage of the battery cells before each discharging process. The discharge cut off voltage (under-voltage) limit was set at 2.5 V. The batteries were then discharged with a constant current (CC) of 6.0 A (≅ 1.15 C). The discharging current was chosen so that a balance between the discharge duration and the maximum temperature rise could be obtained. The infrared camera and the DAQ module were set to start recording and logging the data as the circuit closed. Also, the timer built-in screen recorder software will start timing synchronously. The measurement stops as the battery voltage approaches the discharge under-voltage limit.

3.3.2 Pack-level setup and temperature measurement

For the pack-level tests, the equipment and setups are similar to the cell-level tests but the packing material and the charging method are different. Here, eight LIBs with the same specifications are connected in series in a column. Therefore, instead of using the non-transparent 3D printed pack, acrylic glasses were used for the pack construction to provide optical access for the infrared camera. However, it is found that the infrared light is refracted and could not go through the relatively thick acrylic material, so the battery pack wall facing the infrared camera was made of thin clear plastic film. The battery electrode connectors were made by winding the copper wires onto small bolts. These bolts are

screwed in nuts which were originally glued to the pack by a glue gun, as shown in Figure 3.7. In addition to the advantage of ease of the battery swap as mentioned previously, the electric connector positions can be adjusted by screwing the bolts in and out for different relative heights of the battery cells within the pack. However, it was found that even though the melting point for the glue stick used by the glue gun is about 120 ℃, the connector can be heated to a temperature able to melt the glue material during discharging and hence loosen or even cut off the electric connections. Therefore, the connectors should be clamped onto the battery cells. Figure 3.8 shows the schematics and the picture of the experimental setup for the pack-level tests. It can be seen from Figure 3.8 (b) that each battery cell is clamped.

Figure 3.9 shows the layout of the battery pack and the infrared measurement setups used in the pack-level tests. There were 5 fiber channels placed between each pair of battery cells. The channels are evenly distributed along the width of the battery pack in the pack's transverse direction. Hence, there is no fiber channel covering the battery surface area seen by the camera. Therefore the areal mode infrared measurements can be used. An areal infrared sensing region (Ar, as shown by the yellow regions in Figure 4) is mapped on each battery, in the pattern shown in Figure 3.9 (a). The temperatures are read from the side of the battery pack in the pack-level tests.

As mentioned previously, a charger used in the pack-level test is replaced by a power supply connected to an 8-series battery management system (BMS) circuit board. The schematics of the circuit connections of the battery pack, charger and discharger, and the BMS board is shown in Figure 3.10. The BMS board has four connectors for the battery pack's negative pole (B-), charger negative pole (CH-), discharger negative pole (P-), and

balance cables connecting to each battery cell in the order of the numbers labeled in the figure. It should be noted that: (1) the charger was turned on only when the discharger was shut off, and vice versa; and (2) the order of the balance cable was strictly followed otherwise the resistors on the BMS circuit was burnt.

Since 8 cells were connected in series, the charging and discharging currents were maintained identical to those at the cell-level tests, but the cut-off voltage for the charge and discharge was both multiplied by 8, i.e. 32 V for charging and 20 V for discharging, respectively. The charging and discharging methods and procedures are identical to the cell-level tests (CC-CV for charging and CC for discharging, respectively).

Figure 3.7: Electric connectors glued to the battery pack for the pack-level experiment.

(a)

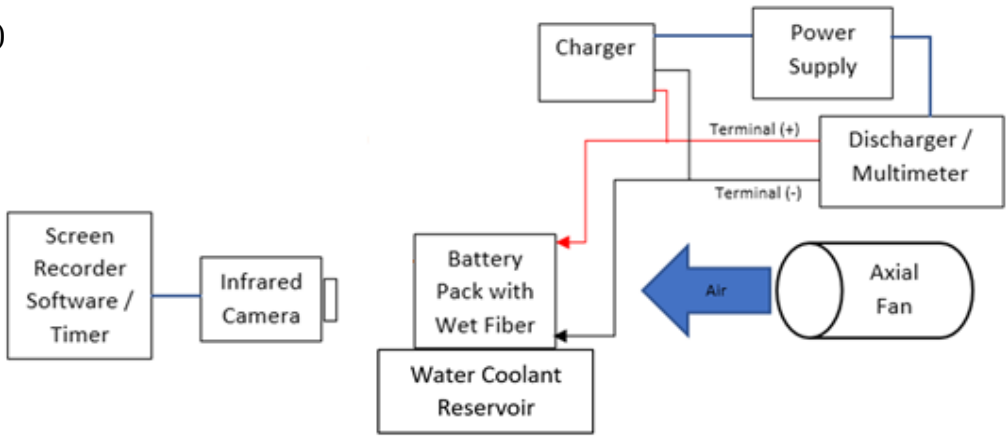

(b)

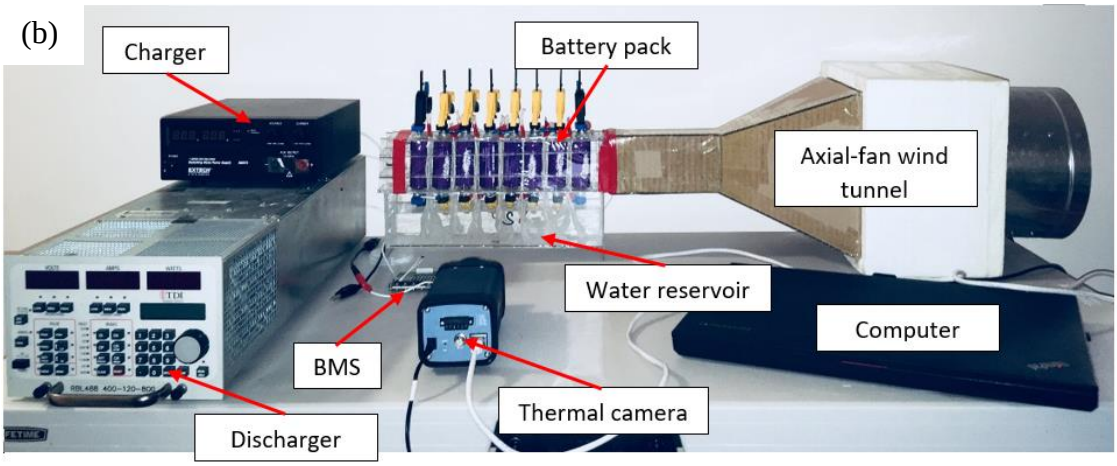

Figure 3.8: Experimental setup for temperature rise and uniformity measurements of the proposed thermal management concept: (a) schematic, and (b) picture of the system.

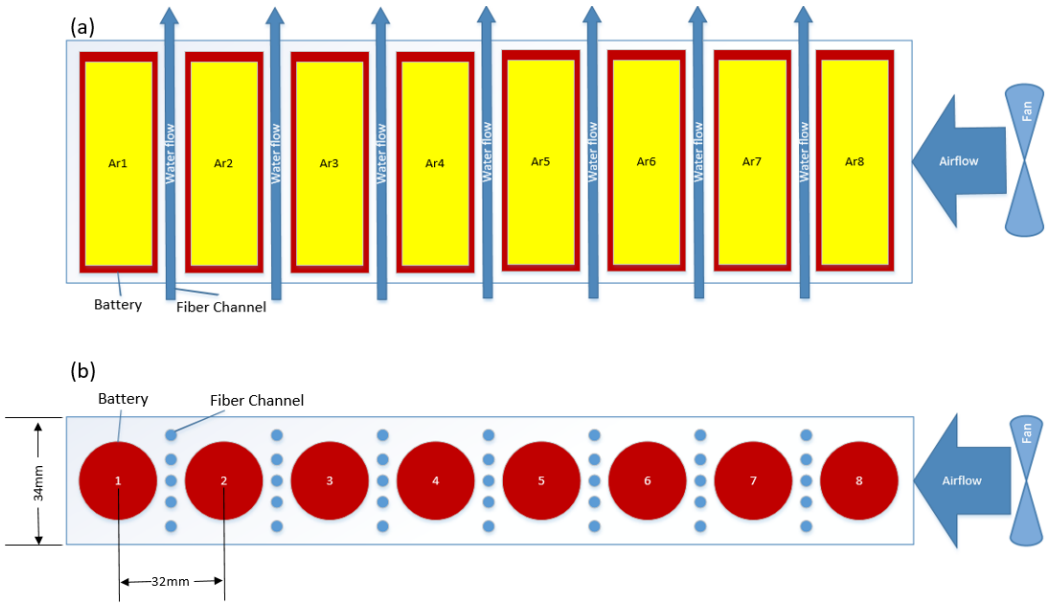

Figure 3.9: Schematic and dimensions of the tested battery pack. (a) side view and (b) top view.

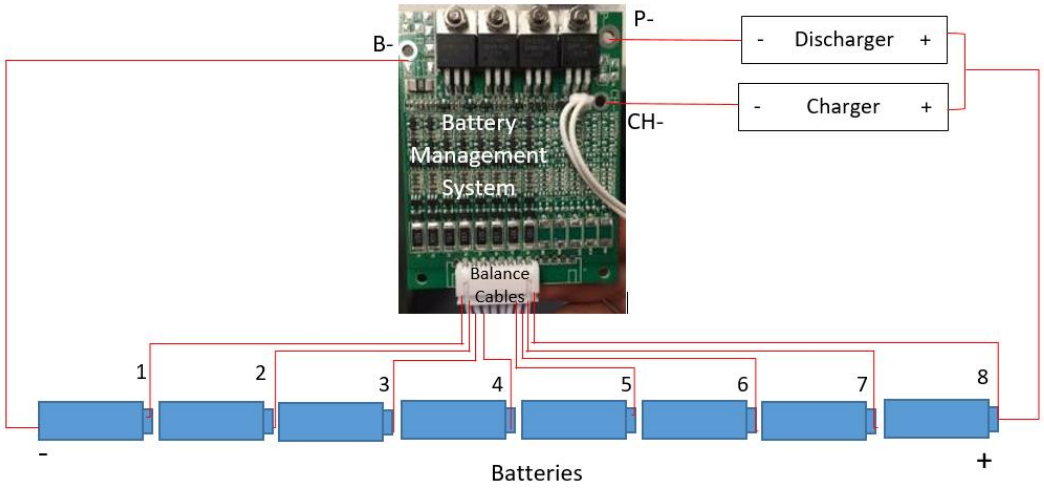

Figure 3.10: Schematics of the battery management system (BMS) circuit connection.

3.3.3 Water evaporation rate measurement

Because of the restriction by the weight scale, the water evaporation rate measurement can only be done in the cell-level. For the water evaporation rate measurement, the battery

pack was made by plastic foam boards because the 3D printed pack is heavier than the upper limit of the weight scale. In the evaporation measurement tests, the battery in the pack was wound with saturated wet fiber channel. The water within the fiber formed no droplet, making sure no water leaks from the fiber channel. The fan was turned on while taking the measurements to eliminate the influence of aerodynamic lift and drag on the battery pack. A set of 10 readings of the initial weight of the pack were taken from the electronic weight scale. Next, the circuit was closed and the infrared recording was started at the same time. After the discharging was done, another set of 10 readings of the final weight were recorded with the fan on. The initial and the final weights were taken by averaging the 10 readings of the corresponding set. The quantity of water evaporated was estimated as the difference between these two averaged weights, and the average vaporization rate is calculated by dividing this difference by the time of measurement:

$$\dot{m} = \frac{m_w - m_d}{t} \tag{3.2}$$

3.3.4 Capillary flow rate and infiltration rate measurement

Capillary infiltration is defined as the distance over which a liquid is driven by the capillary pressure. The infiltration rate was measured by taking a video of the infiltration process. The infiltration height can be estimated by scaling the images of the video with respect to the known height of the battery cell. Hence, the infiltration height at a different time could be plotted.

The measurement of capillary mass flow rate was done only for the contactless hybrid cooling tests, which used pure capillary pressure as the coolant driving force. The weight of 10 dry fiber strips was measured by a sensitive weight scale first, and then the tips of these strips were dipped into the water, meanwhile, the camera recorded the infiltration

process until the strip is wetted thoroughly. The weight of these 10 wet fiber strips was measured and recorded. The water mass flow rate during infiltration is simply calculated as the difference between the dry and wet weight divided by the infiltration time. The flow rate for each fiber was obtained by averaging the resultant flow rate of the 10 fiber strips.

3.4 Error analysis

The uncertainty in the flow rate and vaporization rate measurements is mainly caused by the equipment (i.e. the weight scale) tolerance. Because of the $\pm 0.002\ g$ linearity (accuracy) and $\pm 0.001\ g$ repeatability (precision), the total tolerance for the weight scale is simply summed up as ± 0.003.

The uncertainty in temperature measurement is mainly caused by the measuring equipment, i.e. the thermal camera and thermocouples. Both of the thermal camera and the thermocouples were calibrated with the ambient temperature. The difference (ΔT) by the thermal camera was observed as ± 0.5 ℃ for each measurement position. The ΔT by the thermocouples were observed to be ± 0.2 ℃ after the calibrations through LabVIEW. These are within the reasonable tolerances allowed according to the specifications in Table 3 and Table 4.

The error analysis was performed according to the procedure proposed by Moffat (1988). Any result parameters (R) is determined by a function of a set of measurements (X):

$$R = R(X_1, X_2, X_3, \ldots X_n) \tag{3.3}$$

The actual value of each measurement is $X_i \pm \delta X_i$, where δX_i denotes the uncertainty of each measurement. Hence the resultant uncertainty in each measured parameter X_i can be calculated as:

$$\delta R_{X_i} = \frac{\delta R}{\delta X_i} \delta X_i \tag{3.4}$$

So, the total uncertainty in the result R is calculated as:

$$\delta R = \left(\sum_{i=1}^{N} \delta R_{X_i}^2 \right)^{\frac{1}{2}} \tag{3.5}$$

It is noticed that the δR is an absolute uncertainty with a unit, however, for most of the time the errors would be preferred to be expressed as a relative fraction form which is dimensionless. In particular, if the experimental results are a product of a set of measurements shown in Equation 3.6, then the total relative uncertainty is estimated as Equation 3.7:

$$R = X_1^a X_2^b X_3^c \dots X_n^m \tag{3.6}$$

$$\frac{\delta R}{R} = \left\{ \left(a \frac{\delta X_1}{X_1} \right)^2 + \left(b \frac{\delta X_2}{X_2} \right)^2 + \cdots + \left(m \frac{\delta X_n}{X_n} \right)^2 \right\}^{\frac{1}{2}} \tag{3.7}$$

According to the equations above, as the temperature readings from the thermocouples were verified by the thermal camera reading, the camera measured the temperature by averaging the readings within the whole area by using Equations 3.8 and 3.9:

$$T_{Ar} = \frac{\sum (T_{Ar_{ij}} A_{Ar_{ij}})}{A_{Ar}} \tag{3.8}$$

$$A_{Ar} = (LW)_{Ar} \tag{3.9}$$

Where T_{Ar} is the temperature reading from the thermal camera at any defined area Ar, $T_{Ar_{ij}}$ is the temperature sample detected at the coordinate (i, j) within the area Ar, $A_{Ar_{ij}}$ is the area of the sample segment at the coordinate (i, j) within Ar, and A_{Ar} is the total area

of Ar. Because both of T_{Ar} and A_{Ar} are in a similar form as Equation 3.6, thus the total camera uncertainty within Ar is given as:

$$\frac{\delta T_{Ar}}{T_{Ar}} = \left\{ \left(1 \times \frac{\delta T_{Ar_{ij}}}{T_{Ar_{ij}}} \right)^2 + \left(1 \times \frac{\delta A_{Ar_{ij}}}{A_{Ar_{ij}}} \right)^2 + \left((-1) \frac{\delta A_{Ar}}{A_{Ar}} \right)^2 \right\}^{\frac{1}{2}} \tag{3.10}$$

Where:

$$\frac{\delta A_{Ar}}{A_{Ar}} = \left\{ \left(1 \times \frac{\delta L_{Ar}}{L_{Ar}} \right)^2 + \left(1 \times \frac{\delta W_{Ar}}{W_{Ar}} \right)^2 \right\}^{\frac{1}{2}} \tag{3.11}$$

The term $(\delta T_{Ar_{ij}} / T_{Ar_{ij}})$ is calculated by the absolute bias given by the equipment specification. For example, the maximum relative uncertainty at the sensing position (i, j) for the thermal camera with $\pm$ 2 ℃ maximum tolerance (Table 3) can be given as:

$$\frac{\delta T_{Ar_{ij}}}{T_{Ar_{ij}}} = \pm \frac{2\ [℃]}{T_{Ar_{ij}}\ [℃]} \tag{3.12}$$

However, as the sensing segment areas $A_{Ar_{ij}}$ at different locations within the Ar are unknown, it can be replaced by the relative standard deviation (RSD), which takes both terms of $T_{Ar_{ij}}$ and $A_{Ar_{ij}}$ into considerations:

$$RSD = \frac{s}{\tilde{x}} \times 100\% \tag{3.13}$$

$$s = \sqrt{\frac{\sum\{(\delta T_{Ar_{ij}})^2 A_{Ar_{ij}}\}}{A_{Ar}}} \tag{3.14}$$

Where s is the standard deviation, $\tilde{x}$ is the mean temperature $T_{Ar}$by each independent measurement. The standard deviation of the temperature during each test is shown in Table 6. Hence, Equation 3.10 can be simplified as Equation 3.15. It should be noted that as the no-cooling test was set as the baseline, the uncertainty can only come from the RSD because both the terms $\frac{\delta L_{Ar}}{L_{Ar}}$ and $\frac{\delta W_{Ar}}{W_{Ar}}$ can be set as zero.

$$\frac{\delta T_{Ar}}{T_{Ar}} = \left\{(RSD)^2 + \left(\frac{\delta A_{Ar}}{A_{Ar}}\right)^2\right\}^{\frac{1}{2}} = \left\{(RSD)^2 + \left(\frac{\delta L_{Ar}}{L_{Ar}}\right)^2 + \left(\frac{\delta W_{Ar}}{W_{Ar}}\right)^2\right\}^{\frac{1}{2}} \quad (3.15)$$

Table 6. The standard deviation of temperature by the thermal camera vs. time in different tests

Time (s)	Test standard deviation (℃)			
	No-cooling	Air-cooling	Water-cooling	Hybrid cooling
0	0.13	0.13	0.25	0.31
700	1.26	2.58	1.49	1.44
1400	2.10	3.40	1.76	1.34
2100	2.81	3.81	1.85	1.46

Similarly, for the thermocouple, the uncertainty can be determined by the equipment tolerance from the specification only (Table 4) as the sensing area can be neglected:

$$\frac{\delta T_{tc}}{T_{tc}} = \frac{0.5\ [℃]}{T\ [℃]} \quad (3.16)$$

Table 7. Relative uncertainties vs. time of the thermal camera & thermocouple

Time (s)	Uncertainties [%] (Thermal Camera / Thermocouple)			
	No-cooling	Air-cooling	Water-cooling	Hybrid cooling
0	0.60/2.34	5.39/2.34	4.44/2.26	6.95/2.36
700	2.93/1.16	9.04/1.38	6.30/1.52	8.44/1.77
1400	3.96/0.94	9.71/1.21	6.57/1.41	8.29/1.74
2100	4.73/0.84	10.30/1.15	6.70/1.38	8.44/1.72

Therefore, the overall average uncertainty for the infrared camera and the thermocouple in all the experiments can be estimated as 5.9% and 1.5%, respectively.

Chapter 4: Results and Discussion

In this chapter, the results of the water infiltration rate by capillary pressure and the water vaporization rate measurements are presented. In addition, the rate of battery heat generation measured by the heat flux sensor are reported. Finally, the measurements of the temperature rise and temperature uniformity are analyzed at the cell level and pack level, respectively.

4.1 Capillary infiltration rates and vaporization rates

The material used in the contactless hybrid cooling tests was chosen by comparison among paper towel, candle wick, and carbon fiber tow. As the water reservoir for the test was located underneath the battery pack, an ideal material should be hydrophilic enough to infiltrate the water coolant to the top of the battery pack (height of 55 mm) within a short period by capillary pressure only. It was found that both of the candle wick and the carbon fiber tow was not able to infiltrate the water to the required height, but the paper towel material could drive water to the top of the pack within 5 minutes. Figure 4.1 shows the water coolant infiltration process of the paper material used in the contactless hybrid cooling test.

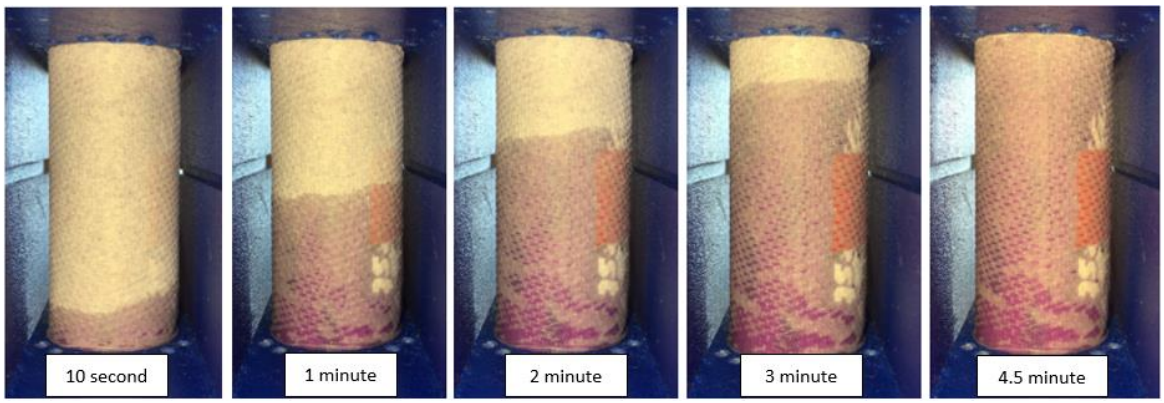

Figure 4.1: Pictures of capillary infiltration test on the paper towel material.

The effect on the infiltration rate by different geometries was also considered. It was found that the infiltration rate for a twisted paper fiber strip, shown in Figure 3.3(b), is much higher than the paper fiber wrap as shown in Figure 4.1. Figure 4.2 compares the time needed for the water coolant to approach the top from the bottom of a single paper fiber strip and a paper wrapping around the battery surface. It shows that water within a fiber strip can flow through the entire length (55 mm) within 70 seconds, while it took more than 3 times that time for the paper wrap of the same height. Additionally, the mean mass of the water infiltrated can be estimated as 0.061 ± 0.003 g/s. Since in the cell-level test, there were 14 fiber strips installed on the battery pack, the total infiltration mass flow rate can be estimated as 0.854 ± 0.042 g/s. For the pack-level test with 35 fiber strips within the battery pack, the total mass flow rate during the infiltration process was estimated as 2.135 ± 0.105 g/s. Both Figures 4.1 and 4.2 are consistent with Equation 2.17, which predicts that the infiltration rate decreases non-linearly over time.

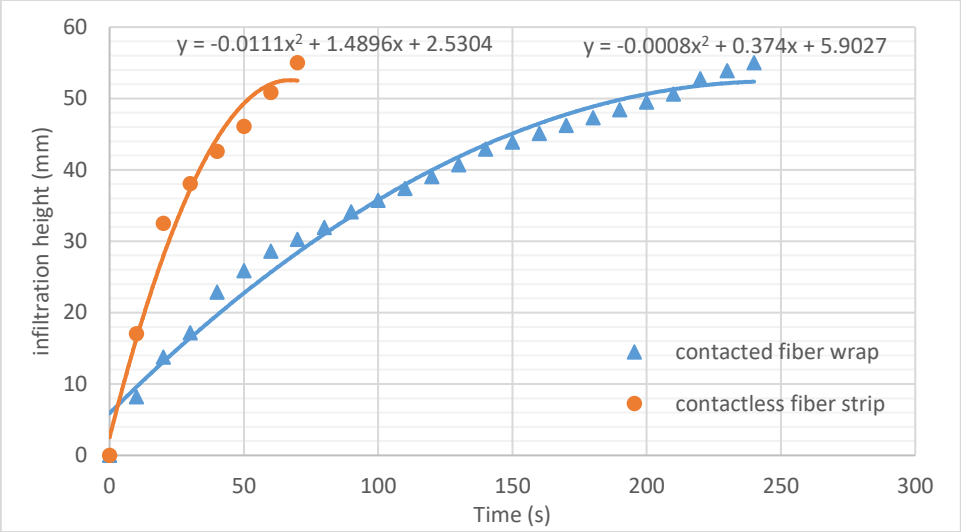

Figure 4.2: Water coolant infiltration over time for a single fiber strip and a paper wrap.

However, as what has been discussed in the Sections 2.3.2 and 2.3.4, the water flow rate within a capillary cooling channel does not only rely on the capillary pressure but also the vaporization. If the vaporization rate cannot go beyond the maximum capillary flow rate, then the water coolant mass flow rate within the fiber channel should be equal to the vaporization rate. The water vaporization rate in a fiber strip under room temperature (21 ℃) was recorded as $1.70\text{e}-04 \pm 5.0\text{e}-06$ g/s ($\cong 1.02e-05\ L/min$) on average, which was much lower than those presented in previous studies (Xu et al., 2017; Lan et al., 2016; Zhao et al., 2015). Hence, it is reasonable to assume that the capillary pressure is high enough to compensate for the water lost by vaporization. Therefore, the fiber channel strip design is suitable for even higher vaporization rates. Additionally, since the latent heat trapped by water vaporization is 2260 J/g, the 14 fiber strips in the cell-level test and the 35 strips in the pack-level test can transfer about 5.22~5.62 Watt and 13.0~14.0 Watt heat by vaporization only, respectively.

4.2 Battery heat generation

The heat flux sensor was used to measure and calculate the heat generation rate on the battery surface. The heat generation rate on the battery surface can be simply calculated by multiply the heat flux by the battery surface area. The heat flux was measured in the no-cooling baseline test. Figure 4.3 shows the heat generation rate on the surface of a single battery cell. As can be seen in the figure, the heat generation is not constant over time. Therefore, an average surface heat generation rate HF_{avg} is calculated by dividing the integration of the given regression equation by the measurement time:

$$HF_{avg} = \frac{\int_0^t hf(t)dt}{t} \tag{4.1}$$

Where hf is the regression expression of the heat generation rate as plotted in Figure 4.3, and HF_{avg} is calculated as about 2.9 Watt over the discharge period of 2100 seconds. This result is consistent with the average LIB heat generation rate presented in previous studies (Shahid and Agelin-Chaab, 2017).

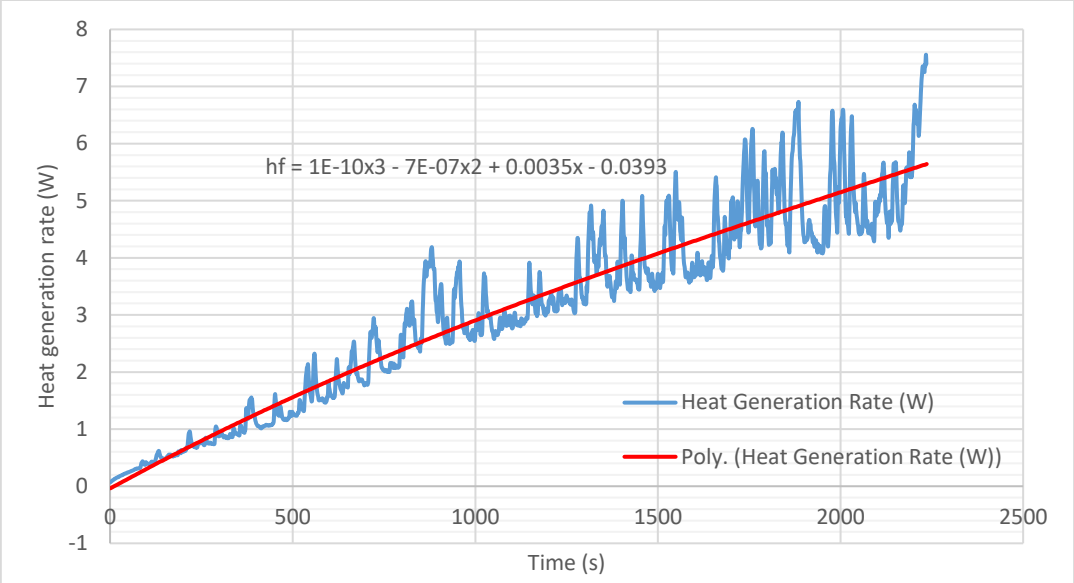

Figure 4.3: Heat generation rate on the surface of a single battery cell.

4.3 Cell-level experiments

4.3.1 Cooling effectiveness

Figure 4.4 shows the plots of the surface temperature measured using the thermocouples under the different cooling methods described above. Due to the tolerances between each individual cell, the length of discharging duration varies between each test but no more than 180 seconds. Therefore, only the temperatures during the first 2100 seconds of discharge are compared. The temperature trends in the figure are comparable to prevous studies (Wu et al., 2013; Saw et al., 2016; Ling et al., 2015). The trend can be explained by the simple equation of conductive heat flux:

$$\Phi_{sur} = k_{T,b} \frac{\partial T}{\partial n} \tag{4.1}$$

As noted earlier, before the discharging process, the temperature for the whole battery was maintained at the ambient temperature. At the beginning of the discharge, a large

temperature gradient was developed as the battery core temperature rose quickly while the surface temperature remained unchanged. At the end of the discharge, a smaller temperature gradient was present as the heat had already been transferred to the outer surface over the period. Therefore, the rate of surface temperature rise was higher at the beginning than the end of discharge.

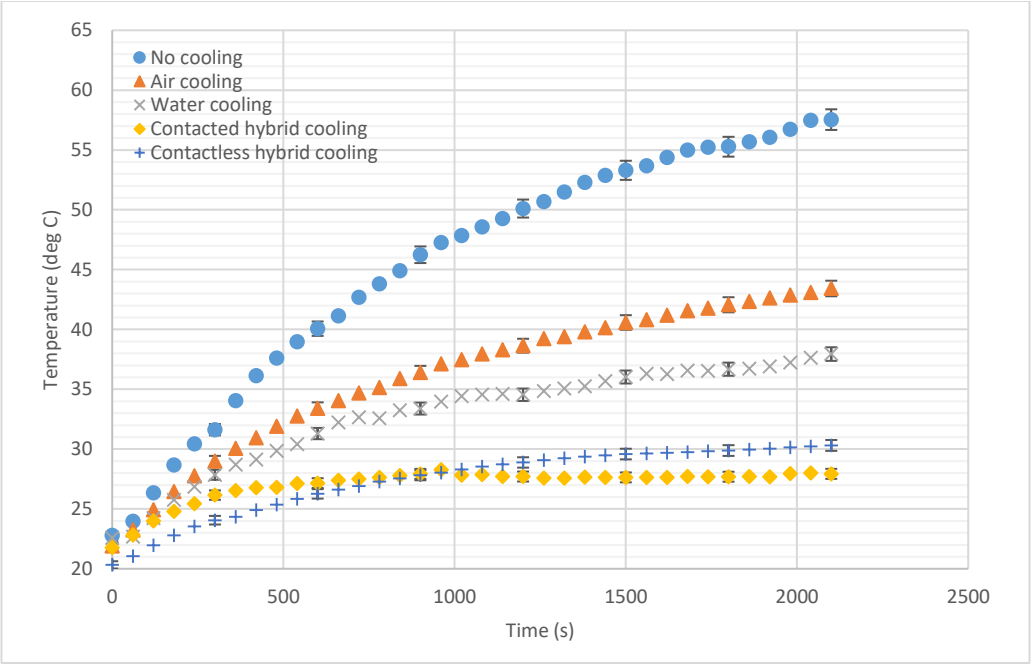

Figure 4.4: Surface temperature change with time during a $1.15C$ constant current discharge followed by a constant current and constant voltage charge starting with $< 0.2C$ load.

The no-cooling case comes with the highest temperature rise as expected. The temperature and its increase rate are all higher than the other cooling methods throughout the test period. After 2100 seconds of discharge, the temperature was as high as 58 ℃ for the no-cooling test. The air-cooling method was able to decrease the highest temperature rise to about 44 ℃, which is a 36.8% improvement compared to the no-cooling baseline case. The water cooling further helps drop the end temperature to 38 ℃, which is an additional 15.6 % improvement over the air-cooling test results. Both of the contacted and

contactless hybrid cooling tests show excellent cooling effectiveness. For the contacted hybrid cooling using a fiber coil, the contacted hybrid cooling was able to maintain the highest temperature under 29 ℃, while the temperature in the contactless hybrid cooling test was a little higher than the contacted case. However, the difference between the two temperatures is only 2 ℃ (28 ℃ in contacted hybrid cooling test and 30 ℃ in the contactless hybrid cooling test, respectively). On the other hand, the temperature for the contacted hybrid cooling test approached its highest temperature in only 800 seconds. The temperature for the contacted hybrid cooling remained unchanged until the end of discharging period at about 2200 seconds, and the temperature for the contactless hybrid cooling hardly increased since 1750 seconds of discharge. Thus, it can be speculated that the temperature can barely rise even if further discharging was applied. The slope of each curve also indicates the outstanding performance of the hybrid cooling method. The temperature rise for both the contacted and contactless hybrid cooling tests are much slower than the rest. Therefore, the hybrid cooling provides the best cooling performance among all the cooling methods shown in the figure. As mentioned previously, the appropriate working temperature for the Li-ion batteries ranges from 25 to 40 ℃. Both of the no-cooling and the air-cooling tests exceeded this limit over the whole battery surface as expected. The temperature contours shown later in Figure 4.9 indicates that the local temperature around the positive tap exceeds this limit even for the water-cooling test. It is only the hybrid cooling method that can maintain the temperature below the operating limit over the entire battery surface. By using the hybrid cooling method, the maximum temperature in the cell level decreased by 82.9% compared to the no-cooling method. Additionally, it decreased by 69.6% and 57.3% compared to the air- and water-cooling,

respectively. Since this is a cell level test, there was no heat accumulation at the battery cylinder wake regions as is the case for a pack level.

4.3.2 Temperature uniformity

The temperature uniformity in this research applies to a cell level uniformity only. None of the previous studies in the open literature suggested a proper uniformity range in the cell level, but it is clear that the temperature deviation should be similar to the recommended pack level uniformity of 5 ℃ (Wu et al., 2013; Shahid and Agelin-Chaab, 2017). Although the uniformity should not be simply defined by the surface temperature, because for a cylindrical battery the assumption of a lumped thermal conductivity is implied (Jaguemont et al., 2016; Zhao et al., 2015; Wu et al., 2013), so the heat is transferred radially from the inside to outside. It therefore implies that a good surface temperature uniformity can be equated to a good overall uniformity.

Figures 4.5 and 4.6 show the temperature contours and the plot of local temperature difference (ΔT) versus discharging time for the no-cooling test as the baseline. All the infrared contours in Figure 4.5 show a good uniformity in the transverse direction. It is also due to the fact that heat is transferred radially from the core to the surface in a cylindrical cell. All the heat cumulating regions are located on the positive tap, while the bottom region has the lowest local temperature. This is due to a higher current density around the positive tap as it is where the current collectors are assembled as shown in Figure 2.3. From Equation 2.7, both terms of the overpotential heat and the reversible entropic heat are correlated with the current density. Therefore, the major temperature non-uniformity is made in battery cell axial (longitudinal) direction.

From the no-cooling baseline, it is found that the maximum local surface temperature can achieve over 67℃ and the lowest was recorded as about 54 ℃ at the end of the discharge (2100 seconds), making a nearly 14 ℃ temperature difference as the maximum non-uniformity. Two linear expressions can be plotted to describe the trend of non-uniformity, since the non-uniformity increased sharply in the first 3 to 5 minutes with a rate of 0.0289 ℃/s and then suddenly slowed down dramatically. This trend is consistent with the results from previous studies (Wu and Zhang, 2014).

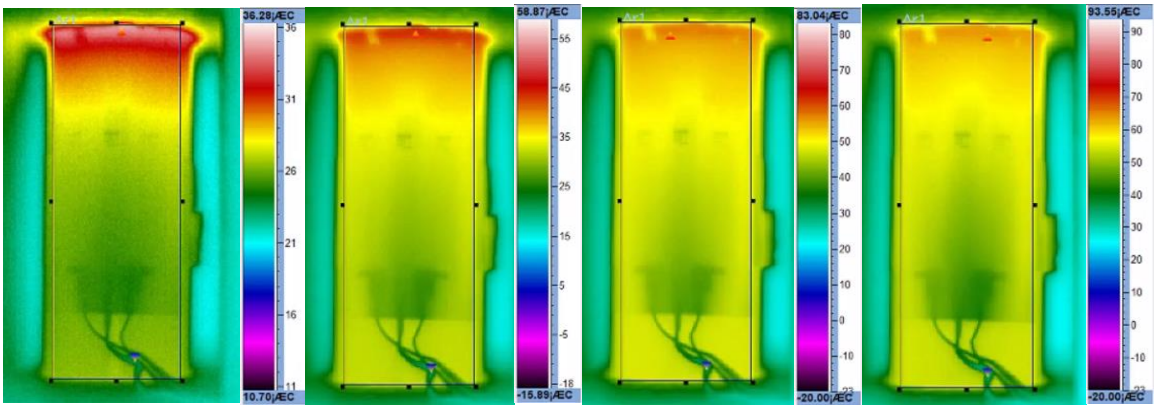

Figure 4.5: Temperature contours for the no-cooling case at different times.

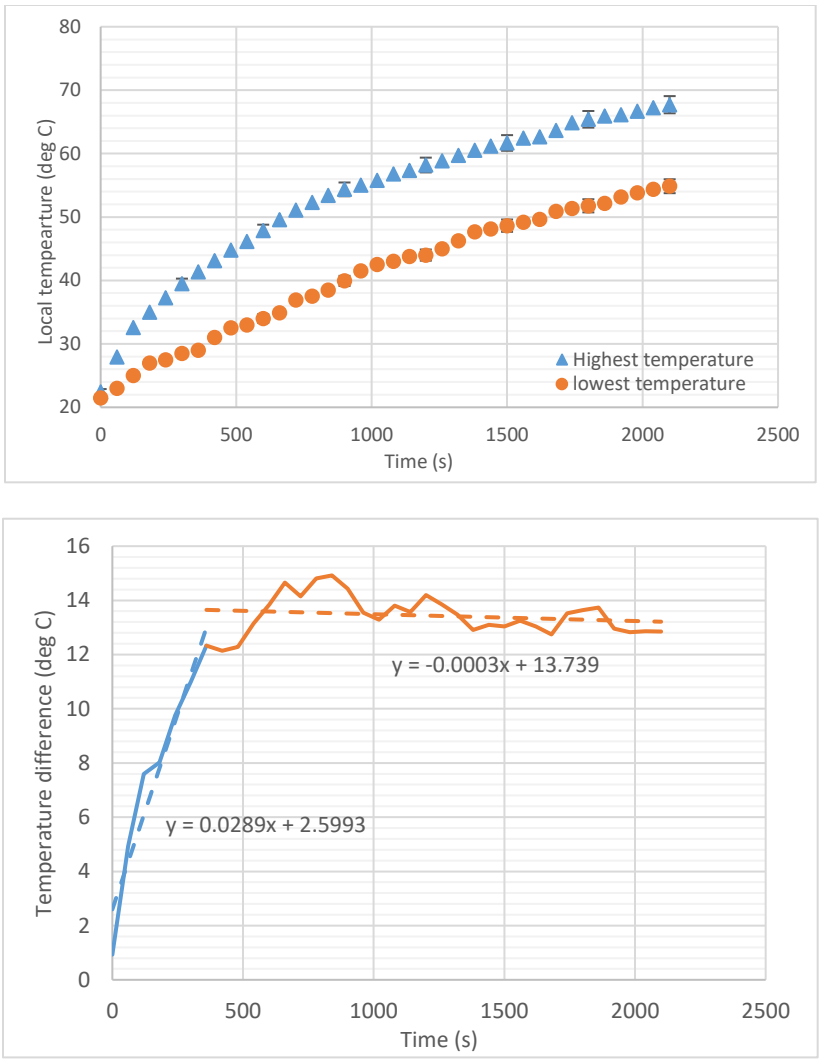

Figure 4.6: Changes of the highest and lowest local temperature (top) and the non-uniformity development (bottom) over time for the no-cooling case.

Figures 4.7 and 4.8 show the temperature contours and the diagrams of changes in local temperatures and the surface temperature non-uniformity for the air-cooling test. The contours are similar to the no-cooling baseline case with the highest local temperature present at the positive electrode region. Since the major temperature non-uniformity occurs in the axial direction, the temperature non-uniformity for the air-cooling test was evaluated by the temperature difference between Sp2 and Sp6 (i.e. $T_{Sp2} - T_{Sp6}$) as shown in Figure

4.7 and denoted as ΔT hereinafter. It is found that during the 2100-second discharge, both the highest and the lowest local temperature increases according to a logarithm function. This is consistent with the data recorded from the thermocouple as shown in Figure 4.4. Also, similar to the no-cooling baseline, two linear expressions can be used to describe the trends of non-uniformity as shown in Figure 4.8. The ΔT increases sharply to 3.8℃ with a rate of $0.0211℃/s$ in the first 180 seconds, then increases with a slower rate of 0.0008 $℃/s$ to around 5.6℃ at the end of the test. The result indicates that even though the air-cooling method cannot cool down the cell efficiently, it can still significantly decrease the temperature non-uniformity to half of that for the no-cooling case. However, as what has been mentioned previously, such a good result was produced from the cell-level test, without taking consideration of factors such as head loss along the air duct and heat accumulation at the battery wake region. Hence the temperature uniformity under the air-cooling could be worse in pack-level applications.

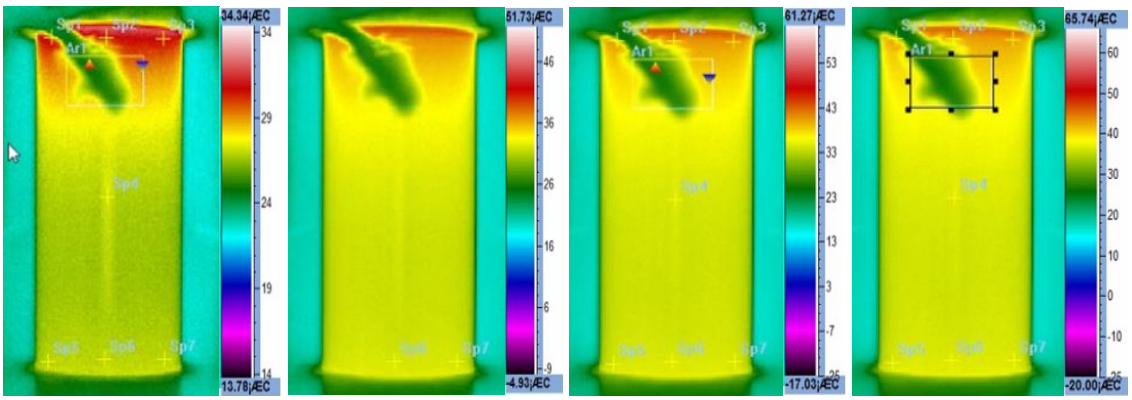

Figure 4.7: Temperature contours for the air-cooling case at different times.

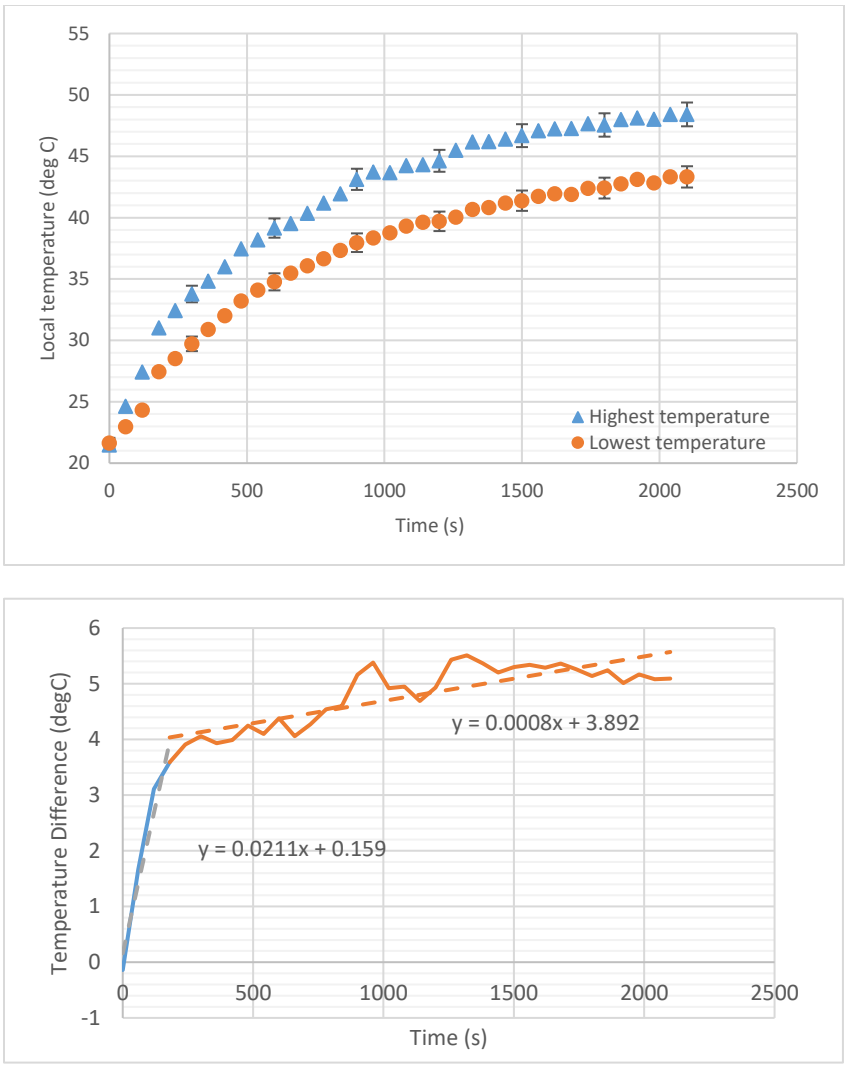

Figure 4.8: Changes of the highest and lowest local temperature (top) and the non-uniformity development (bottom) over time for the air-cooling case.

The temperature contours and the non-uniformity trends for the water-cooling test are also similar to the previous tests as shown in Figures 4.9 and 4.10, respectively. The ΔT was evaluated by the temperature difference between Sp2 and Sp6. The ΔT increased sharply for the first 180 seconds and then became more gradual afterwards. The increase rate was estimated as 1.584 ℃/min for the first 3 minutes, and dropped to 0.0358 ℃/min afterwards. Estimating from the regression equation, the ΔT approached about 5 ℃ in the

first 180 seconds with a increasing rate estimated as $0.0264\,℃/s$, and then slowly increased to about 6 ℃ at the end of the discharge cycle. The highest local surface temperature was about 44 ℃, which exceeded the upper limit of the allowable working temperature of 40 ℃ as mentioned earlier (Shahid and Agelin-Chaab, 2017). One can see that the non-uniformity observed from the air- and the water-cooling test did not significantly differ from each other. In fact, the difference between them is only 0.4℃, which is much lower than the equipment tolerance (2% of camera reading, or 1.16℃) and implies that there is basically no differences in the results. The result implies that the water cooling can provide high cooling efficiency, but it doesn't improve the temperature uniformity significantly over the air cooling case.

Substantial condensation water was also observed on the side wall of the battery pack in the water-cooling test, as shown in Figure 4.11. Since the same fiber channel was used for both the water- and the hybrid cooling tests, vaporized moisture in the water-cooling test could also be released into the ambient and condense onto any cold surface nearby. This condensation proved the existence of considerable evaporation and hence the latent heat removed by the phase-change effect. The condensation was not observed in the hybrid cooling test since the moisture was removed by the forced air convection.

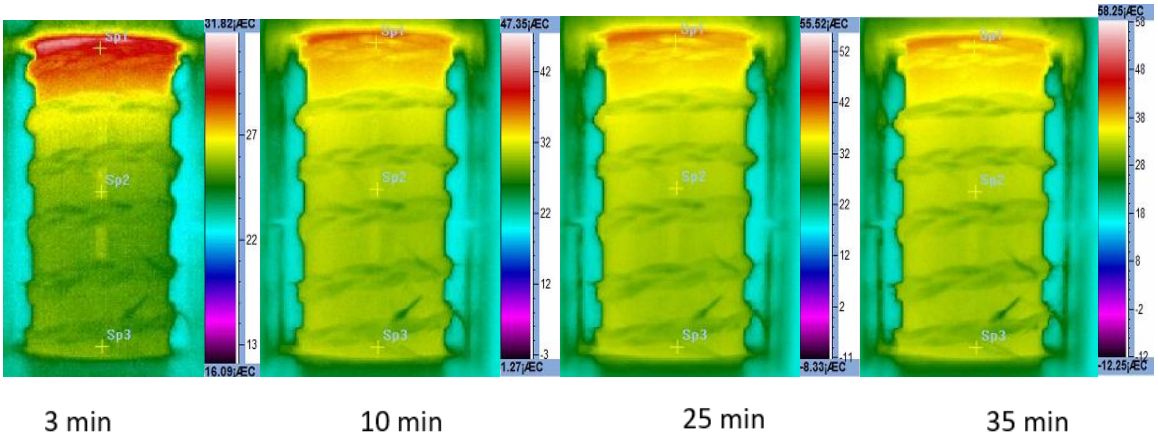

Figure 4.9: Temperature contour obtained by the thermal camera at different times for the water-cooling test.

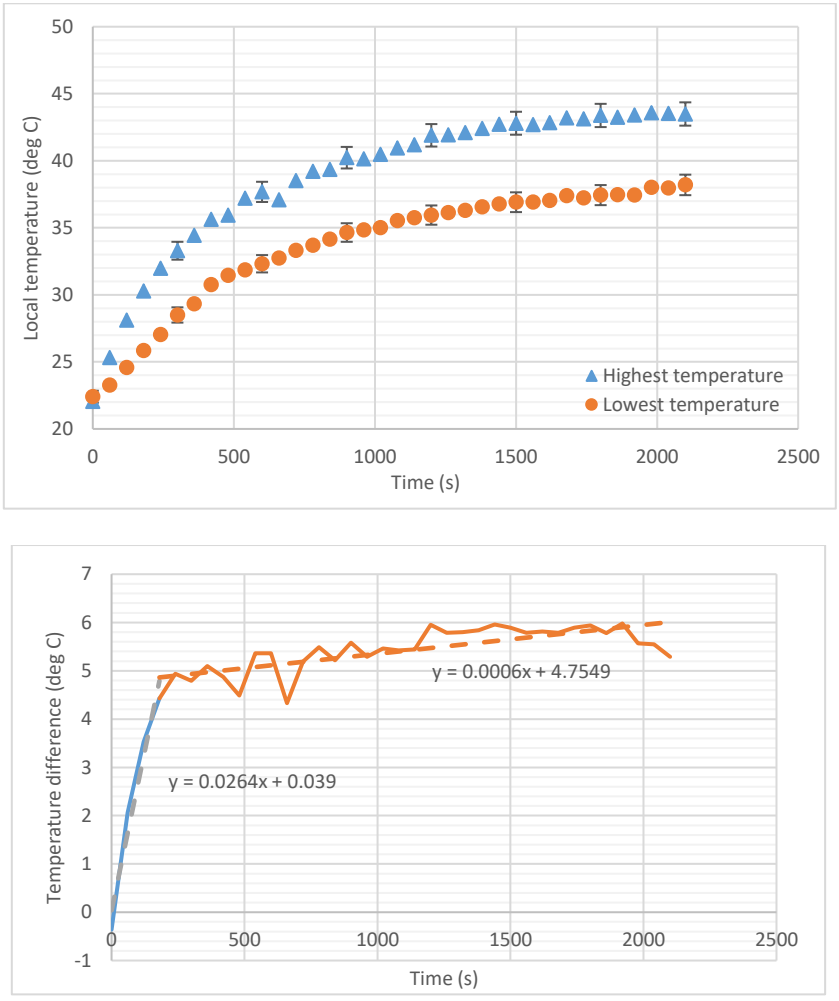

Figure 4.10: Changes of the highest and lowest local temperature (top) and the non-uniformity development (bottom) over time for the water-cooling case.

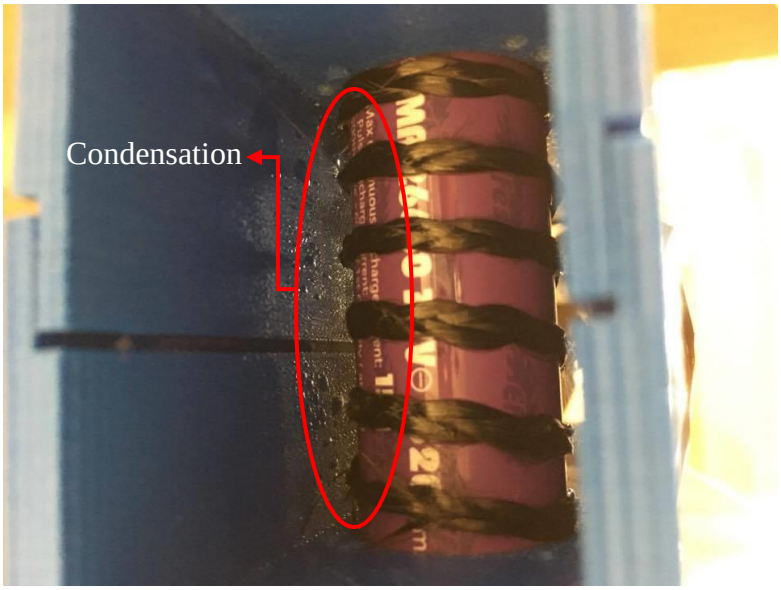

Figure 4.11: Photo of condensation on the battery pack wall observed in the water-cooling test.

Figures 4.12 and 4.13 show the temperature contours and the trends of non-uniformity for the contacted hybrid cooling test. Trends of ΔT similar to the previous cases can be observed. The contacted hybrid cooling test improves the uniformity further than any of the previous cases. After 180 seconds of temperature rise with similar increasing rate of 0.0286 ℃/s, the ΔT slightly fluctuated around 4℃, which made it the only case that could maintain the ΔT under the limit of 5℃. The result showed that the hybrid cooling method has great potential to improve the temperature uniformity.

It can be found that, no mater which cooling method mentioned above was used, the initial increasing rates of the temperature non-uniformity are very similar (range from 0.021 to 0.029 ℃/s). Therefore, a general linear expression for initial surface temperature non-uniformity under similar test conditions may be given as:

$$\Delta T_{initial} = 0.025t \pm C \tag{4.2}$$

Where t is time in seconds, C is a small magnitude of correction coefficient.

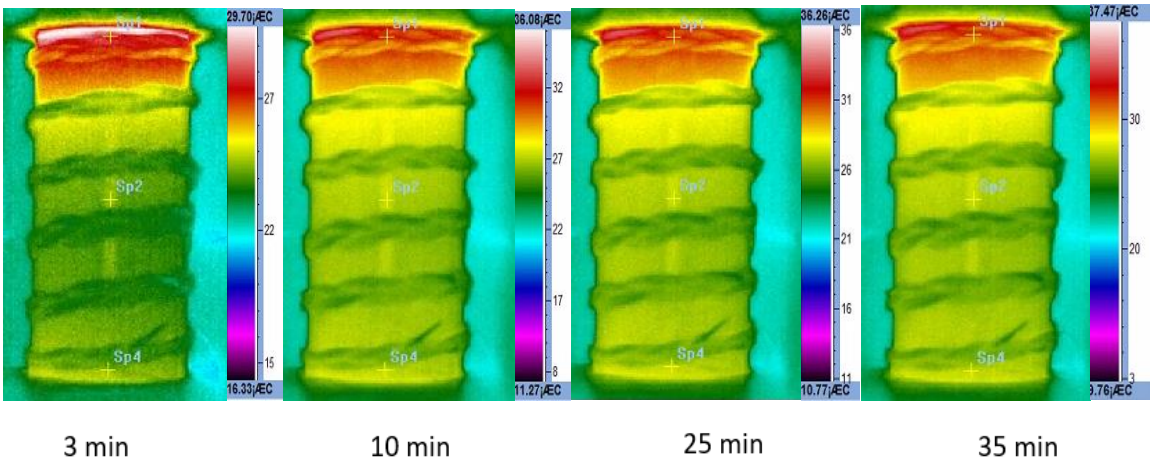

Figure 4.12: Temperature contour obtained by the thermal camera at different times for the contacted hybrid cooling test.

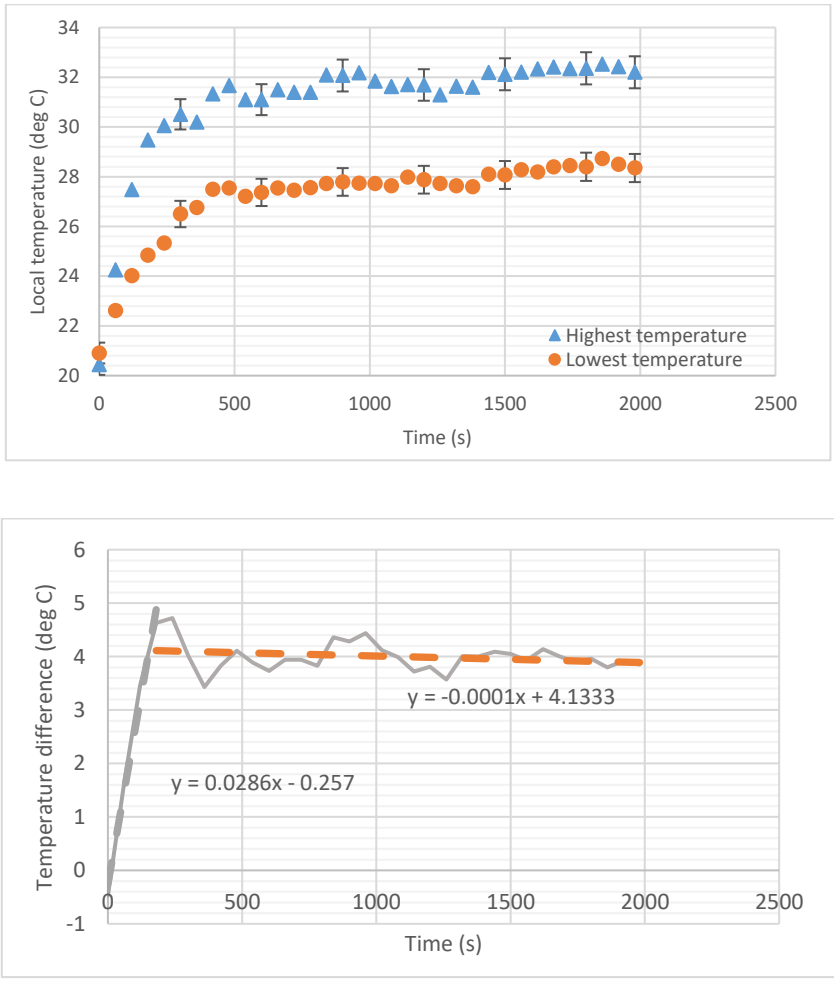

Figure 4.13: Changes of the highest and lowest local temperature (top) and the non-uniformity development (bottom) over time for the contacted hybrid-cooling case.

Figures 4.14 and 4.15 show the temperature contours and the diagrams of changes in local temperatures and the surface temperature non-uniformity for the contactless hybrid cooling test. The temperature uniformity of the contactless hybrid cooling method shows much improvement even compared to the contacted hybrid cooling. The non-uniformity increase was much smaller and a 3rd order polynomial regression equation rather than two linear expressions could be plotted. It was found that the maximum non-uniformity only approached 2.1℃ at $t = 1350$ seconds and remained unchanged to the end of the discharge. The highest local surface temperature was recorded lower than 33 ℃, which is well below the allowable upper limit of the working temperature (Shahid and Agelin-Chaab, 2017). Therefore, the hybrid cooling method can meet the requirements mentioned above, and provide the best temperature uniformity among all the tested methods.

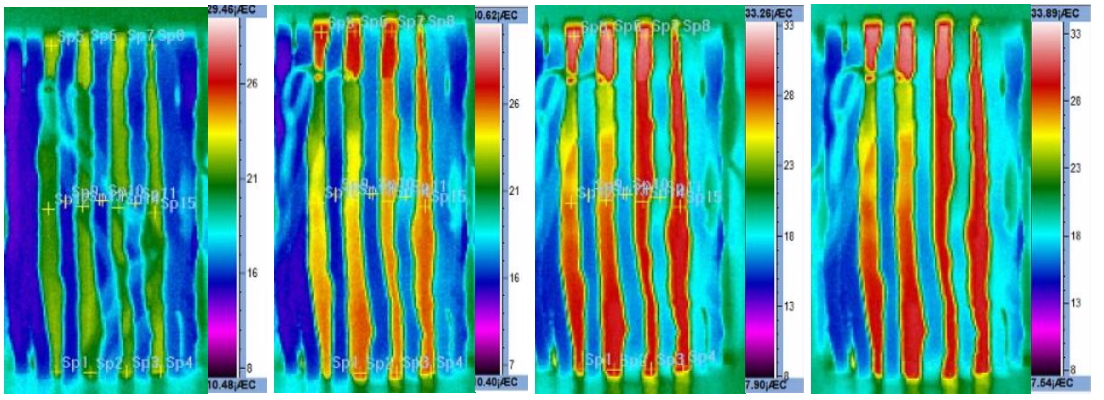

Figure 4.14: Temperature contours for the hybrid cooling case at different times.

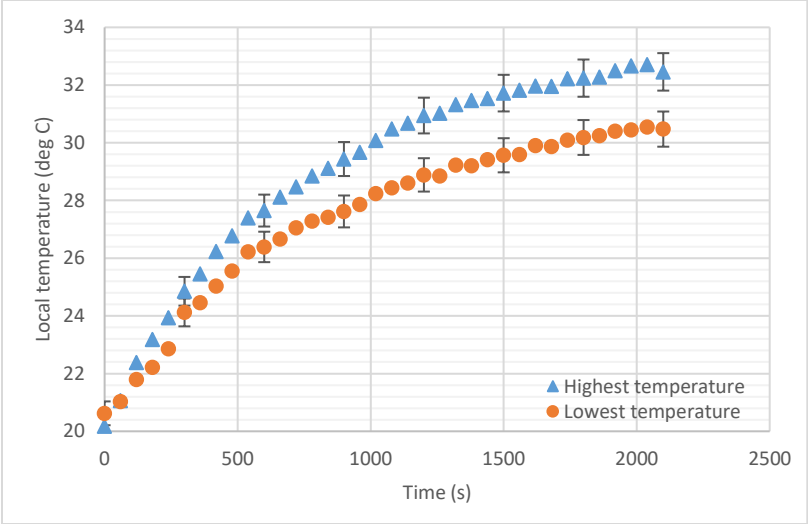

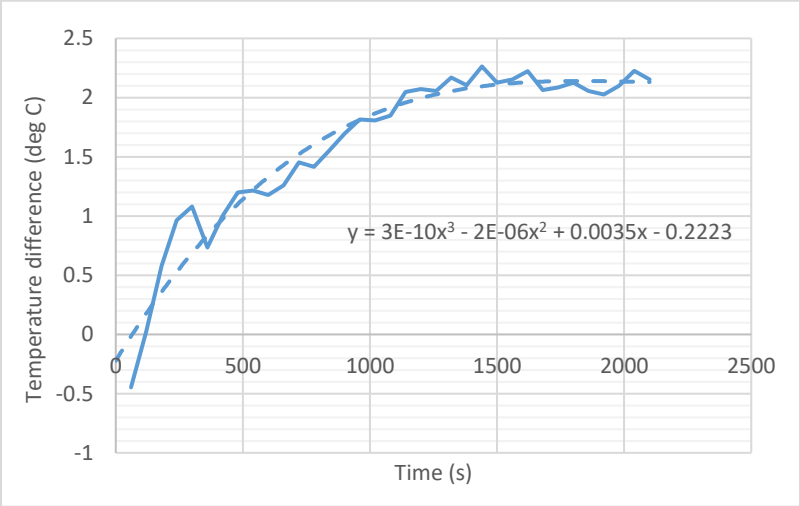

Figure 4.15: Changes of the highest and lowest local temperature (top) and the non-uniformity development (bottom) over time for the hybrid cooling case.

The good performance from both of the contacted and the contactless hybrid cooling proves what the researchers expected. The hybrid cooling method has a much higher cooling efficiency than both of the air cooling and the water cooling methods, because of the latent heat extracted by the water vaporization. In addition, the hybrid cooling method offers a much better temperature uniformity than the other methods presented.

4.4 Pack-level experiments

From the cell-level test results presented in Section 4.3, the outstanding performance of the proposed hybrid cooling method was observed. However, the contactless design which has a similar cooling effectiveness but a much better temperature uniformity compared to the contacted design is further studied and discussed for the pack-level. Additionally, since the battery is an electric power unit, the contactless design is better from a safety perspective. On the other hand, without the contact of the fiber with the cell surface, the water cooling testing was not possible. Therefore, a set of pack level tests including no-cooling baseline, air-cooling, and contactless hybrid cooling methods are discussed in this section.

4.4.1 Cooling effectiveness

Figure 4.16 shows the temperature contours at the end of discharge and plots of average surface temperatures for each cell versus time for the no-cooling conditions. One can observe that the cell in the middle of the pack has the highest surface temperature. The temperature diminishes from the mid-pack to both the inlet and outlet locations. This makes sense since the cells at both ends have no heat accumulation from an adjacent cell, while the cell in the middle suffers the most heat transferred from both sides of the battery pack. The plot shows results that are consistent with this conclusion. During the entire discharging period, Ar4 located in the middle of the pack shows the most aggressive temperature rise, and it records a final temperature of 60 ℃. Ar3, Ar5, and Ar6 have rising temperature trends that are almost identical. The final reading for these three cells is about 57 ℃. The cells Ar2 and Ar7 at the locations indicated share a similar temperature trend, and the final temperature is recorded as 55 ℃ and 52 ℃, respectively. The cells Ar1 and

Ar8 at the locations indicated have the lowest rate of temperature increase because they are furthest to the central location and have the most heat accumulation. The final temperatures at these locations are identical for both cells and are recorded as 47 ℃. Therefore, all the cells in this no-cooling test under 1.15C discharging rate have final temperatures that are over the limit of 40 ℃. In fact, the temperatures start exceeding this limit after only 14 minutes of discharge.

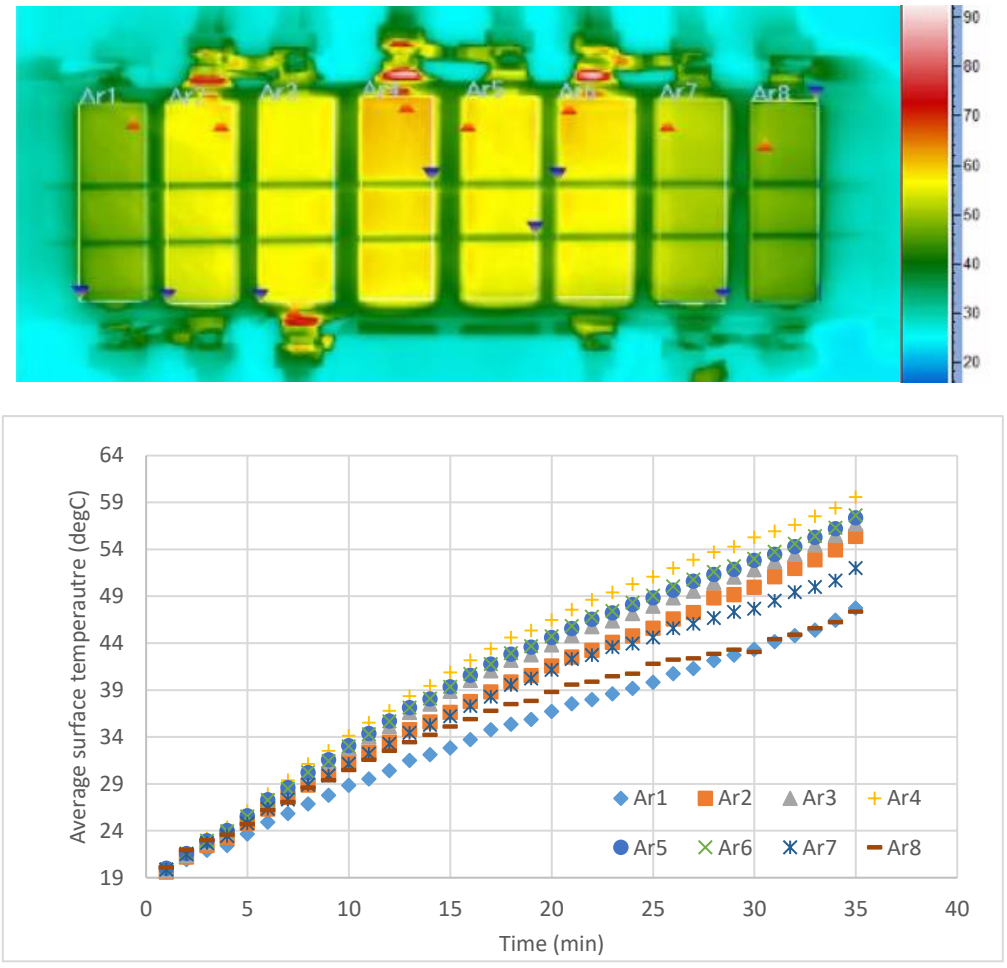

Figure 4.16: Temperature contours (top) at the end of discharge and plots of average surface temperature (bottom) for each cell versus time for the no-cooling baseline.

Figure 4.17 shows the temperature contours at the end of discharge and plots of the average surface temperature for each cell versus time for the air-cooling conditions. Compared to Figure 5, the heat accumulation region (yellow) has shifted towards the pack outlet because the heat can only be transferred from the inlet to outlet under unidirectional airflow. For each cell location except for Ar1, the hot spots, indicated by the red triangle indexes occurs at the leeward side due to the wake there. This conclusion is consistent with previous studies (Yang et al., 2015). The cell with the highest temperature for this cooling case is Ar2 instead of Ar4 for the no-cooling case. The rest of the cells have nearly identical temperature trends and final temperature readings with the final temperatures around 38 ℃ to 39 ℃. For the first 5 minutes of discharge, cell Ar1 had a rate of temperature rise similar to Ar8 that is located at the pack inlet, because there is no heat built up in the pack. The temperature rose sharply after 5 minutes and reached to a final value of 38 ℃, which is close to the value at Ar6. Cells Ar7 and Ar8 located around the pack inlet have the working temperature lower than the rest, and the final temperature for Ar8 is recorded as 30 ℃. Air cooling successfully lowers the working temperature for each cell under the limit of 40 ℃. However, the temperatures for 6 out of the 8 cells are very close to the limit of 40 ℃. This strongly suggests that the temperature will exceed this limit even at a slightly higher discharge C-rate.

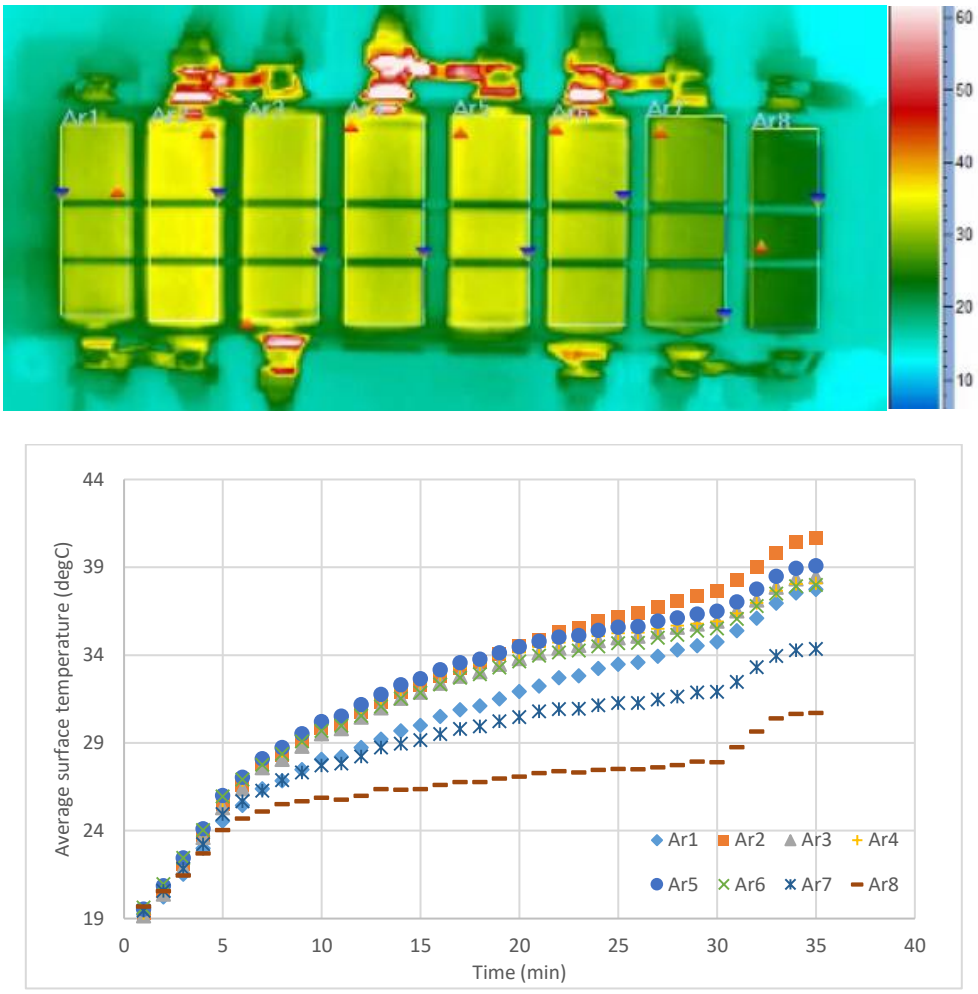

Figure 4.17: Temperature contours (top) at the end of discharge and plots of average surface temperature (bottom) for each cell versus time for the air cooling method.

Figure 4.18 shows the temperature contours at the end of discharge and plots of average surface temperature for each cell versus time for the hybrid cooling conditions. From the contour, it is hard to tell which cell has the highest working temperature, and the color distributes more evenly compared to the two previous tests. The indexes for the hot spots are more random. From the plot, both Ar2 and Ar4 have the highest final temperature of 32 ℃. The rate of Ar2 temperature rise for the first 20 minutes of discharge is same as the majority of the cells, because of the same reason previously discussed. After 20 minutes,

the heat built up in the pack is transferred to the outlet, and hence Ar2 shows a sharp temperature rise until at the end of discharge. Ar1, Ar3, Ar5, Ar6, and Ar7 have similar temperature trends. The final temperatures for all of them were recorded as 0 ℃. It can be observed that Ar1 at the outlet position comes with the lowest temperature for the first 15 minutes, but its final temperature ranks the third highest among all the cells. This is consistent with the temperature trend of Ar2. Ar8 which is located at the inlet without heat transfer from other cells presents the lowest rate of temperature rise and the lowest final temperature (28 ℃). The hybrid cooling method successfully maintains the working temperature for all the cells under the 40 ℃ limit, and the highest temperature is still 8 ℃ lower than this limit, making more room for further discharging and higher discharge C-rate.

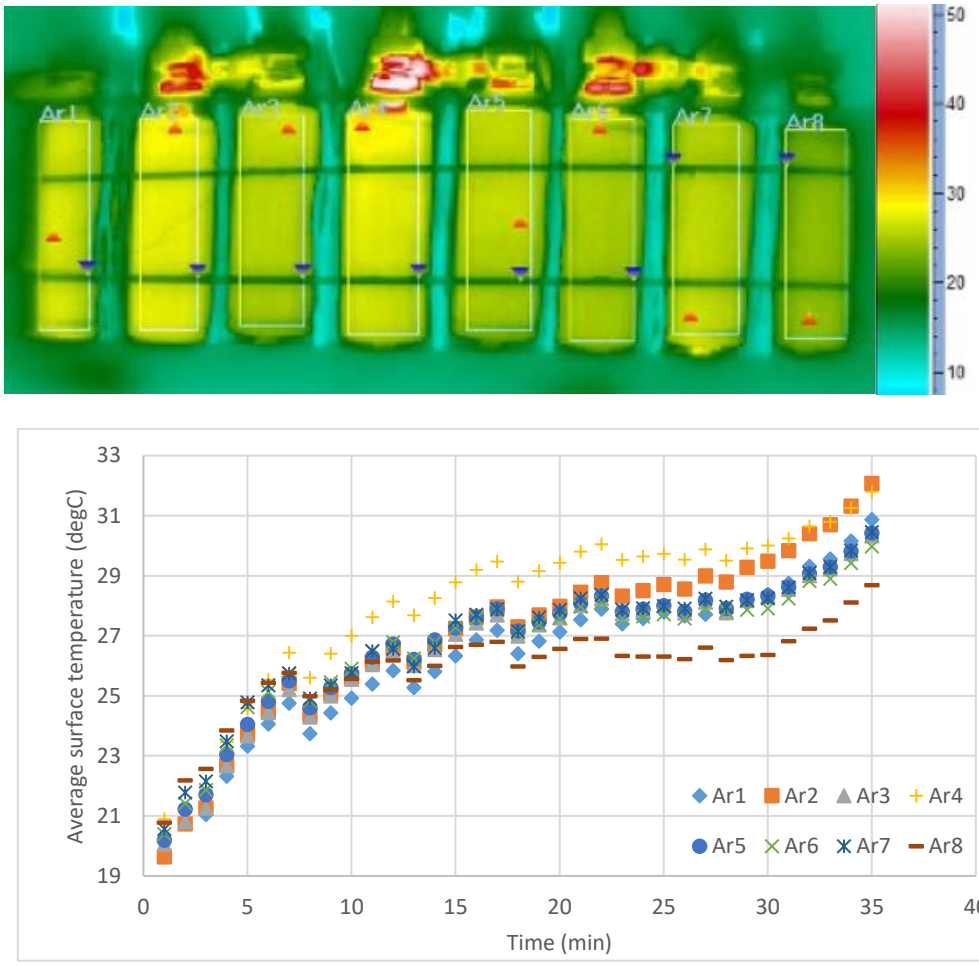

Figure 4.18: Temperature contours (top) at the end of discharge and plots of average surface temperature (bottom) for each cell versus time for the hybrid cooing method.

Figure 4.19 shows the pack level average temperature during the discharges under the three conditions shown. The temperature in the no cooling test reaches 54 ℃ which is 14 ℃ over the limit. By simply using the air cooling method, the final temperature was lower by 50% to 37 ℃. The proposed hybrid cooling method can further lower the final temperature to only 30 ℃. This is a 71% improvement compared to the no-cooling baseline.

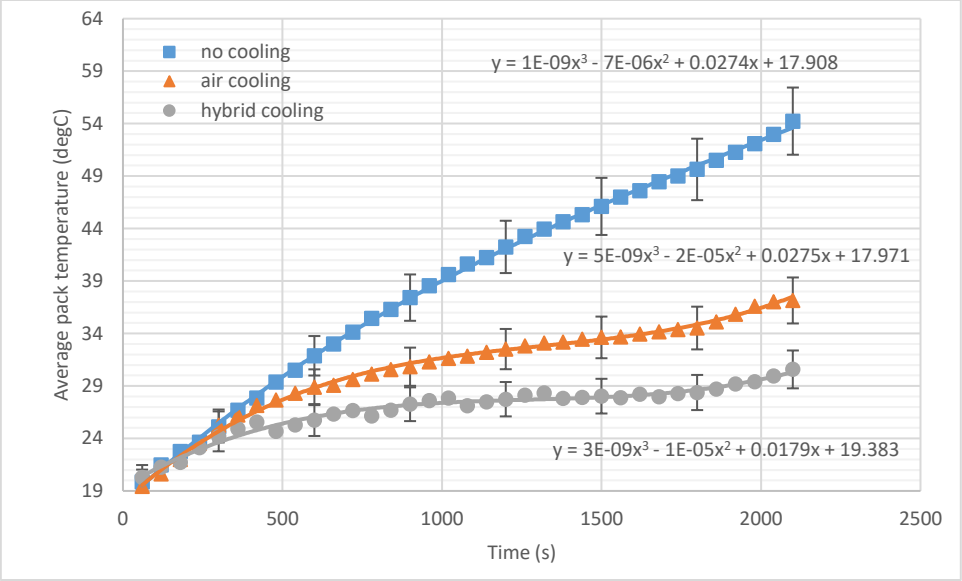

Figure 4.19: Average pack temperature comparison among the three cooling types: no cooling, air cooling, and hybrid cooling.

4.4.2 Temperature uniformity

Figure 4.20 shows the trends of pack-level temperature non-uniformity for the three cooling conditions. It was mentioned previously that the maximum pack-level non-uniformity should not exceed 5 ℃ (Shahid and Agelin-Chaab, 2017).

The non-uniformity of no-cooling condition exceeds this limit after only 9 minutes of discharge, and it ends up with 12.3 ℃. Even though the air cooling can lower the final working temperature by 50%, it does not work well from the temperature uniformity perspective. The final non-uniformity is shown as 10 ℃, which is only a 16.7% improvement and is double the 5 ℃ limit. In fact, the hybrid cooling method stands out in this comparison. The non-uniformity in the hybrid cooling test retains under 4 ℃. The final reading is shown as only 3.4 ℃. Therefore, the proposed hybrid cooling method improves the temperature uniformity by 72.4% compared to the baseline.

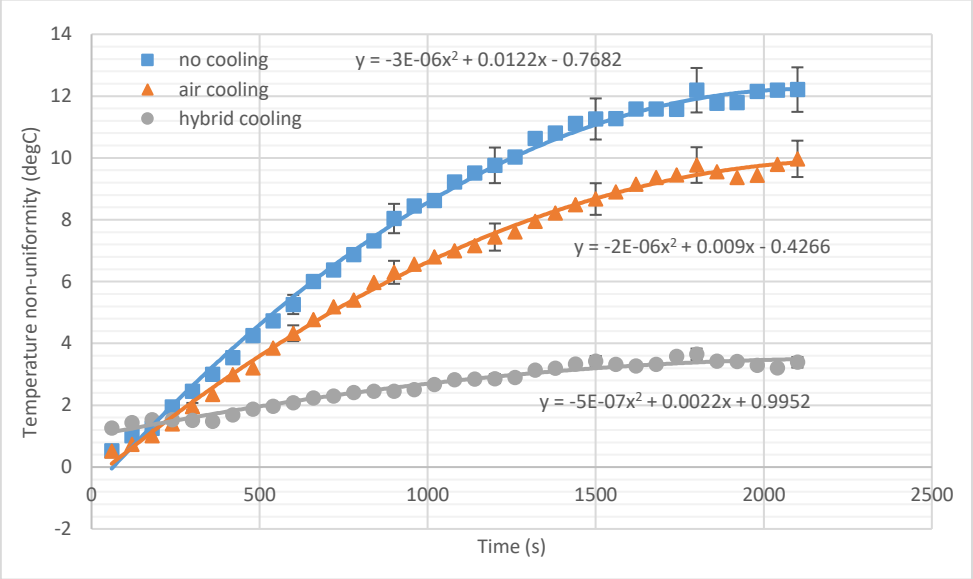

Figure 4.20: Temperature non-uniformity comparison among the three cooling types: no cooling, air cooling, and hybrid cooling.

Chapter 5: Conclusion and Recommendation

This thesis proposed a new hybrid cooling method for electric batteries. The proposed concept was examined experimentally and was successfully verified. In this chapter, the results obtained in this research are summarized and conclusions drawn. In addition, the contributions made by the thesis will be presented. Furthermore, recommendations are provided for the future optimization and final design of the concept.

5.1 Summary of results

The results obtained and discussed earlier show that the proposed concept has a higher cooling efficiency and much better temperature uniformity over the battery pack. The concept was able to maintain both the maximum working temperature and non-uniformity below the recommended temperature limits. However, most of the conventional techniques were found unable to achieve the target cooling effectiveness or temperature uniformity at either the cell-level or pack-level tests. Under a discharging rate just over 1C which is far below the rate used in many previous studies, the air-cooling method could not effectively maintain the temperature under the limit of 40 ℃. The water-cooling barely maintained the average surface temperature under the limit for both of the pack- and cell-level tests, but the local temperatures around the positive poles of the cells were still observed to be higher than the 40 ℃ limit. This suggests a high probability of failure at a higher discharging rate.

At the cell level, the contacted hybrid cooling was able to maintain the highest cell surface temperature at around 30 ℃. For the same location of each cell, the contacted hybrid cooling method was able to decrease the highest temperature rise by 82.9%, 69.6%, and 57.3% compared to that of the no-cooling, the air-cooling, and the water-cooling tests,

respectively. The maximum cell-level temperature difference in the contacted hybrid cooling test was reported as 4 ℃. However, the contactless hybrid cooling was able to decrease the maximum average surface temperature from 55 ℃ in the no-cooling case to only 30 ℃; a 73.5% reduction in temperature. It also decreases the maximum temperature by 60.9% and 47.0% compared to air- and water-cooling, respectively. In addition, the proposed concept produced the lowest temperature non-uniformity (≅ 2℃) among all the tests, which is 85.7% reduction from the baseline and well below the threshold value.

At the pack level, the contactless hybrid cooling provided more than 70% improvement in both the cooling efficiency and the temperature uniformity compared to the no-cooling baseline. It achieved a 20% improvement in the cooling efficiency and a 56% improvement in the temperature uniformity compared to the air-cooling. These results are significant considering that the fact that they were achieved under proof of concept experiments which were not optimized at all. Therefore, there is a great potential for further improvement in the proposed hybrid cooling concept.

5.2 Contribution

A new concept of thermal cooling of electric batteries was developed and proven in this thesis. The concept utilizes any combination of conductive, convective, and evaporative phase change cooling effects. The concept uses series of hydrophilic fiber channels containing the water coolant that are exposed to the convective coolant to extract the latent heat from the battery. There is nothing like it in the open literature.

The new concept is innovative in nature for the following reasons:

- The water coolant used in this system is driven purely by capillary effect from the fiber material. This eliminates the need for pumps, tubing and heat

exchangers for the coolant recirculation. It also means a huge weight reduction and hence energy saving for electric vehicle applications.

- The water coolants are environmentally friendly and non-toxic, hence they can be released to the ambient with no damage to the environment and human health.
- The concept may recycle the air-condition condensate so the water coolant can be instantly consumed as it is generated and hence adds negligible weight to the vehicle.

5.3 Limitations of the Thesis

Since the experiments conducted were aimed to proof the concept proposed, only specific testing conditions were conducted. The temperatures of coolants and ambient were kept constant at room temperature but this is not the case in real life operating conditions. Additionally the vaporization rate must vary depending on different ambient coolant temperatures and humidity. However, the analysis of the effects of temperature and humidity on vaporization was not included in this study. Furthermore, the air flow velocity was fixed around 0.8 m/s, and the influence of the fan power on cooling performance was not examined. Finally, it should be noted that only 26650 cylindrical LMO batteries are used in this study. Furthermore, only the air duct design with inline layout using vertical unidirectional flow is investigated. Lastly, the pitch between each battery cell within the pack is fixed as 32 mm longitudinally and 34 mm transversely.

5.4 Recommendations for future works

From the limitation mentioned in the previous sections, it is recommended that the proposed idea be further examined with a wider range of test conditions experimentally or using computational fluid dynamics techniques. Some optimization work should also be done focusing on manipulating different geometries and battery layouts. In addition, empirical correlations linking the battery working temperature and temperature non-uniformity can be developed using a lot of data from further repeated experiments and simulations.

Publications from Thesis

Wei, Y. and Agelin-Chaab, M. (2018). Experimental investigation of a novel hybrid cooling method for lithium-ion batteries. *Applied Thermal Engineering*, 136, pp.375-387.

Wei, Y. and Agelin-Chaab, M. (2018). Development and Experimental Analysis of a Hybrid Cooling Concept for Electric Vehicle Battery Packs Submitted to *Applied Energy*.

Wei, Y. and Agelin-Chaab, M. (2018). Experimental Study of a Thermal Cooling Technique for Cylindrical Batteries. Submitted to *Jounal of Energy Storage*.

Wei, Y. and Agelin-Chaab, M. (2018). Novel Hybrid Cooling Concept for Battery Thermal Management Design. Accepted paper in the 5th International Conference on Fluid Flow, Heat and Mass Transfer (FFHMT'18).

References

Abdul-Quadir, Y., Laurila, T., Karppinen, J., Jalkanen, K., Vuorilehto, K., Skogström, L. and Paulasto-Kröckel, M. (2014), "Heat generation in high power prismatic Li-ion battery cell with LiMnNiCoO2cathode material", International Journal of Energy Research, 38(11), pp.1424-1437.

Batteryuniversity.com. (2018), "Types of Battery Cells; Cylindrical Cell, Button Cell, Pouch Cell", [online] Available at: http://batteryuniversity.com/learn/article/types_of_battery_cells [Accessed 3 Jan. 2018].

Beard, K. and Pruppacher, H. (1971). A Wind Tunnel Investigation of the Rate of Evaporation of Small Water Drops Falling at Terminal Velocity in Air. Journal of the Atmospheric Sciences, 28(8), pp.1455-1464.

Cao, R., Li, X., Chen, S., Yuan, H. and Zhang, X. (2017), "Fabrication and characterization of novel shape-stabilized synergistic phase change materials based on PHDA/GO composites", *Energy*, 138, pp.157-166.

Chapman, L. (2007). Transport and climate change: a review. Journal of Transport Geography, 15(5), pp.354-367.

Ciez, R. and Whitacre, J. (2017). Comparison between cylindrical and prismatic lithium-ion cell costs using a process based cost model. Journal of Power Sources, 340, pp.273-281.

Digital.ni.com (2017), "Thermocouple Accuracy Table by Type and Temperature - National Instruments", [online] Available at: http://digital.ni.com/public.nsf/websearch/BA5B756B76BB595A862579B3008168C0?opendocument& Submitted&&node=133020_US [Accessed 25 Mar. 2018].

Eckert, J., Silva, L., Costa, E., Santiciolli, F., Dedini, F. and Corrêa, F. (2017). Electric vehicle drivetrain optimisation. IET Electrical Systems in Transportation, 7(1), pp.32-40.

Efestpower.com (2017), "Efest IMR 26650 5000mAh 45A flat top battery - Batteries – EFEST", [online] Available at: http://www.efestpower.com/index.php?ac=article&at=read&did=448.

El-Ladan, A. and Haas, O. (2015), "Fan-pad evaporative battery cooling for hybrid electric vehicle thermal management", In: *IET Conference Proceedings*. Stevenage: The Institution of Engineering & Technology, p.7.

Emadi, A., Young Joo Lee and Rajashekara, K. (2008). Power Electronics and Motor Drives in Electric, Hybrid Electric, and Plug-In Hybrid Electric Vehicles. IEEE Transactions on Industrial Electronics, 55(6), pp.2237-2245.

Fan, L., Khodadadi, J.M. and Pesaran, A.A. (2013), "A parametric study on thermal management of an air-cooled lithium-ion battery module for plug-in hybrid electric vehicles", Journal of Power Sources, 238, pp. 301–312.

Fathabadi, H. (2014), "High thermal performance lithium-ion battery pack including hybrid active-passive thermal management system for using in hybrid/electric vehicles", Energy, 70, pp.529-538.

Finegan, D., Darcy, E., Keyser, M., Tjaden, B., Heenan, T., Jervis, R., Bailey, J., Vo, N., Magdysyuk, O., Drakopoulos, M., Di Michiel, M., Rack, A., Hinds, G., Brett, D. and Shearing, P. (2018). Thermal Runaway: Identifying the Cause of Rupture of Li-Ion Batteries during Thermal Runaway (Adv. Sci. 1/2018). Advanced Science, 5(1), p.1870003.

Florides, G. and Christodoulides, P. (2009). Global warming and carbon dioxide through sciences. *Environment International*, 35(2), pp.390-401.

Fueleconomy.gov, U. S. Environmental Protection Agency and U.S. Department of Energy, 2015-01-06. Retrieved 2015-11-06.

Fujita, A., Kurose, R., and Komori, S. (2010), “Experimental study on effect of relative humidity on heat transfer of an evaporating water droplet in air flow”, International Journal of Multiphase Flow, 36(3), pp.244-247.

Gu, W. and Wang, C. (2000), “Thermal-Electrochemical Modeling of Battery Systems”, Journal of The Electrochemical Society, 147(8), p.2910.

He, F. and Ma, L. (2015), “Thermal management of batteries employing active temperature control and reciprocating cooling flow”, International Journal of Heat and Mass Transfer, 83, pp.164-172.

He, F., Akram AMS, A., Roosien, Y., Tao, W., Geist, B. and Singh, K. (2017), “Reduced-order Thermal Modeling of Liquid-cooled Lithium-ion Battery Pack for EVs and HEVs”, Chrysler Tech Center,1000 Chrysler Dr, Auburn Hills, MI, USA.

Iliev, O., Printsypar, G. and Rief, S. (2013). A two-dimensional model of the pressing section of a paper machine including dynamic capillary effects. Journal of Engineering Mathematics, 83(1), pp.81-107.

Jaguemont, J., Boulon, L. and Dubé, Y. (2016), “A comprehensive review of lithium-ion batteries used in hybrid and electric vehicles at cold temperatures”, Applied Energy, 164, pp.99-114.

Julien, C., Mauger, A., Zaghib, K. and Groult, H. (2014), “Comparative Issues of Cathode Materials for Li-Ion Batteries”, Inorganics, 2(1), pp.132-154.

Kendall, K., Kendall, M., Liang, B. and Liu, Z. (2017). Hydrogen vehicles in China: Replacing the Western Model. International Journal of Hydrogen Energy, 42(51), pp.30179-30185.

Kizilel, R., Sabbah, R., Selman, J.R., and Al-Hallaj, S. (2009), “An alternative cooling system to enhance the safety of Li-ion battery packs”, Journal of Power Sources, 194(2), pp. 1105–1112.

Lan, C., Xu, J., Qiao, Y. and Ma, Y. (2016), “Thermal management for high power lithium-ion battery by mini-channel aluminum tubes”, Applied Thermal Engineering, 101, pp.284-292.

Lanz, A., Heffel, J., and Messer, C. (2001), “Hydrogen fuel cell engines and related technologies”, Palm Desert, Calif: College of the Desert, Energy Technology Training Center.

Leroux, G., Mendes, M., Stephan, L., Pierrès, N, L., Wurtz, E. (2015), “An innovative cooling system based on evaporation from a porous tank”, 14th Conference of International Building Performance Simulation Association, Hyderabad, India, Dec. 7-9, 2015.

Li, H., Lu, Y., Zhang, J. and Wang, T. (2013). Trends in road freight transportation carbon dioxide emissions and policies in China. Energy Policy, 57, pp.99-106.

Ling, Z., Wang, F., Fang, X., Gao, X. and Zhang, Z. (2015), “A hybrid thermal management system for lithium-ion batteries combining phase change materials with forced-air cooling”, Applied Energy, 148, pp. 403–409.

Liu, G., Ouyang, M., Lu, L., Li, J. and Han, X. (2014), “Analysis of the heat generation of lithium-ion battery during charging and discharging considering different influencing factors”, Journal of Thermal Analysis and Calorimetry, 116(2), pp.1001-1010.

Liu, Y., Ouyang, C., Jiang, Q. and Liang, B. (2015), “Design and parametric optimization of thermal management of lithium-ion battery module with reciprocating air-flow”, Journal of Central South University, 22(10), pp. 3970–3976.

Liu, Z., Wang, Y. and Zhang, J. (2014), “Shortcut computation for the thermal management of a large air-cooled battery pack”, Applied Thermal Engineering, 66(1-2), pp. 445–452.

Lygte-info.dk. (2018). Test of Efest IMR26650 5200mAh (Purple) 2016. [online] Available at: http://lygte-info.dk/review/batteries2012/Efest%20IMR26650%205200mAh%20(Purple)%202016%20UK.html [Accessed 25 Mar. 2018].

Mahamud, R. and Park, C. (2011), “Reciprocating air flow for Li-ion battery thermal management to improve temperature uniformity”, Journal of Power Sources, 196(13), pp. 5685–5696.

Mahamud, R. and Park, C. (2013), “Spatial-resolution, lumped-capacitance thermal model for cylindrical Li-ion batteries under high Biot number conditions”, Applied Mathematical Modelling, 37(5), pp.2787-2801.

Mahmoudzadeh Andwari, A., Pesiridis, A., Rajoo, S., Martinez-Botas, R. and Esfahanian, V. (2017). A review of Battery Electric Vehicle technology and readiness levels. Renewable and Sustainable Energy Reviews, 78, pp.414-430.

Maier, J. (2016). ChemInform Abstract: Review - Battery Materials: Why Defect Chemistry?. ChemInform, 47(5), p.no-no.

Messina, C. (2015). Cylindrical Vs Prismatic Cells. [online] Lithiumion-batteries.com. Available at: https://www.lithiumion-batteries.com/cylindrical-vs-prismatic-cells.php [Accessed 24 Mar. 2018].

Moffat, R. (1988), "Describing the uncertainties in experimental results", Experimental Thermal and Fluid Science, 1(1), pp.3-17.

Oceania.ohaus.com. (2018). Pioneer® Precision Electronic Balance, PA153. [online] Available at: https://oceania.ohaus.com/en-OC/Products/Balances-Scales/Precision-Balances/Pioneer-Precision/PA153 [Accessed 25 Mar. 2018].

Panchal, S., Khasow, R., Dincer, I., Agelin-Chaab, M., Fraser, R., and Fowler, M. (2017), "Thermal design and simulation of mini-channel cold plate for water-cooled large sized prismatic Lithium-ion battery", Applied Thermal Engineering, Vol 122, 80-90.

Panchal, S., Mathewson, S., Fraser, R., Culham, R., and Fowler, M. (2015), "Thermal management of lithium-ion pouch cell with indirect liquid cooling using dual cold plates approach", SAE International Journal of Alternative Powertrains, Vol 4, 293-307.

Park, H. (2013), "A design of air flow configuration for cooling lithium-ion battery in hybrid electric vehicles", Journal of Power Sources, 239, pp. 30–36.

Philip, John R. (1957), "The theory of infiltration: 4. Sorptivity and algebraic infiltration equations", Soil Science. 84: 257–264.

Rahman, M., Rahman, H., Mahlia, T. and Sheng, J. (2016). Liquid cooled plate heat exchanger for battery cooling of an electric vehicle (EV). IOP Conference Series: Earth and Environmental Science, 32, p.012053.

Rao, Z. and Wang, S. (2011), "A review of power battery thermal energy management", Renewable and Sustainable Energy Reviews, 15(9), pp. 4554–4571.

Sasmito, A., Birgersson, E., and Mujumdar, A. (2012), "A novel flow reversal concept for improved thermal management in polymer electrolyte fuel cell stacks", International Journal of Thermal Sciences, 54, pp.242-252.

Saw, L., Ye, Y. and Tay, A. (2013), “Electrochemical–thermal analysis of 18650 Lithium Iron Phosphate cell”, Energy Conversion and Management, 75, pp.162-174.

Saw, L.H., Ye, Y., Tay, A.A.O., Chong, W.T., Kuan, S.H. and Yew, M.C. (2016), “Computational fluid dynamic and thermal analysis of lithium-ion battery pack with air cooling”, Applied Energy, 177, pp. 783–792.

Schlapbach, L. (2009). Hydrogen-fuelled vehicles. Nature, 460(7257), pp.809-811.

Sensor, T. and Engineering, O. (2018). Thin Film Heat Flux Sensor Models HFS-3 and HFS-4. [online] Omega.ca. Available at: https://www.omega.ca/pptst_eng/HFS-3_HFS-4.html [Accessed 25 Mar. 2018].

Shah, K., McKee, C., Chalise, D. and Jain, A. (2016), “Experimental and numerical investigation of core cooling of Li-ion cells using heat pipes”, Energy, 113, pp.852-860.

Shahid, S. and Agelin-Chaab, M. (2017), “Analysis of Cooling Effectiveness and Temperature Uniformity in a Battery Pack for Cylindrical Batteries”, Energies, 10(8), p.1157.

Shan, C., Guanghui, G. and Fangfang, L. (2013), “Study on the performance of LiMn2O4 using spent Zn–Mn batteries as manganese source”, Journal of Solid State Electrochemistry, 18(6), pp.1495-1502.

Smith, K. and Wang, C. (2006), “Power and thermal characterization of a lithium-ion battery pack for hybrid-electric vehicles”, Journal of Power Sources, 160(1), pp.662-673.

SPI Corp (2017), “XP 5000 Radiometric Infrared Camera”, [online] Available at: https://www.x20.org/product/raz-ir-pro-xp-5000-infrared-camera/.

Stanford Graduate School of Business. (2008). It's About Forty Years Until the Oil Runs Out. [online] Available at: https://www.gsb.stanford.edu/insights/its-about-forty-years-until-oil-runs-out [Accessed 27 Feb. 2018].

Sun, H. and Dixon, R. (2014), “Development of cooling strategy for an air-cooled lithium-ion battery pack”, Journal of Power Sources, 272, pp. 404–414.

Tanda, G. (2015). The use of infrared thermography to detect the skin temperature response to physical activity. Journal of Physics: Conference Series, 655, p.012062.

Tong, W., Somasundaram, K., Birgersson, E., Mujumdar, A.S. and Yap, C. (2016), "Thermo-electrochemical model for forced convection air cooling of a lithium-ion battery module", Applied Thermal Engineering, 99, pp. 672–682.

Toyota to launch Mirai in Sweden, Norway to boost European fleet. (2016). Fuel Cells Bulletin, (4), pp.2-3.

Turza, R. and Füri, B. (2017), "Experimental Measurements of the Water Evaporation Rate of a Physical Model", Slovak Journal of Civil Engineering, 25(1).

Wang, Q., Ping, P., Zhao, X., Chu, G., Sun, J. and Chen, C. (2012). Thermal runaway caused fire and explosion of lithium ion battery. Journal of Power Sources, 208, pp.210-224.

Wang, T., Tseng, K.J., Zhao, J., and Wei, Z. (2014), "Thermal investigation of lithium-ion battery module with different cell arrangement structures and forced air-cooling strategies", Applied Energy, 134, pp. 229–238.

Wu, B., Li, Z. and Zhang, J. (2014). Thermal Design for the Pouch-Type Large-Format Lithium-Ion Batteries: I. Thermo-Electrical Modeling and Origins of Temperature Non-Uniformity. Journal of the Electrochemical Society, 162(1), pp.A181-A191.

Wu, B., Yufit, V., Marinescu, M., Offer, G., Martinez-Botas, R. and Brandon, N. (2013), "Coupled thermal–electrochemical modelling of uneven heat generation in lithium-ion battery packs", Journal of Power Sources, 243, pp.544-554.

Xu, J., Lan, C., Qiao, Y. and Ma, Y. (2017), "Prevent thermal runaway of lithium-ion batteries with mini-channel cooling", Applied Thermal Engineering, 110, pp.883-890.

Yang, N., Zhang, X., Li, G. and Hua, D. (2015), "Assessment of the forced air-cooling performance for cylindrical lithium-ion battery packs: A comparative analysis between aligned and staggered cell arrangements", Applied Thermal Engineering, 80, pp. 55–65.

Zhao, C., Kang, W., Zhao, S. and Shen, Q. (2011), "Hydrazine–hydrothermal synthesis of pure-phase O-LiMnO2 for lithium-ion battery application", Micro & Nano Letters, 6(10), p.820.

Zhao, J., Rao, Z., and Li, Y. (2015), "Thermal performance of mini-channel liquid cooled cylinder based battery thermal management for cylindrical lithium-ion power battery", Energy Conversion and Management, 103, pp.157-165.

Zhao, R., Zhang, S., Liu, J. and Gu, J. (2015), “A review of thermal performance improving methods of lithium ion battery: Electrode modification and thermal management system”, Journal of Power Sources, 299, pp.557-577.

Appendices

Appendix A: Cell-level local temperature comparison between windward and leeward under air-cooling

The temperatures at the center of the projected area of the battery windward and leeward were compared under the cell-level air-cooling test, with the same setup presented in this thesis except for the ambient temperature and the discharging rate (1C instead of 1.15C). The ambient temperature was recorded at around 24 ℃ due to the measurement taken in summer time of 2017. Figure A.1 shows the temperature recorded by the T-type thermocouples at different locations. It can be found that even under a unidirectional airflow, the windward and leeward temperature barely made any differences in the cell-level tests. Even though the highest temperature recorded is shown as 51 ℃ only, the temperature contour captured at 27'30" of discharge, shown as Figure A.2, indicates that the temperature around the battery's positive pole was about 60 ℃.

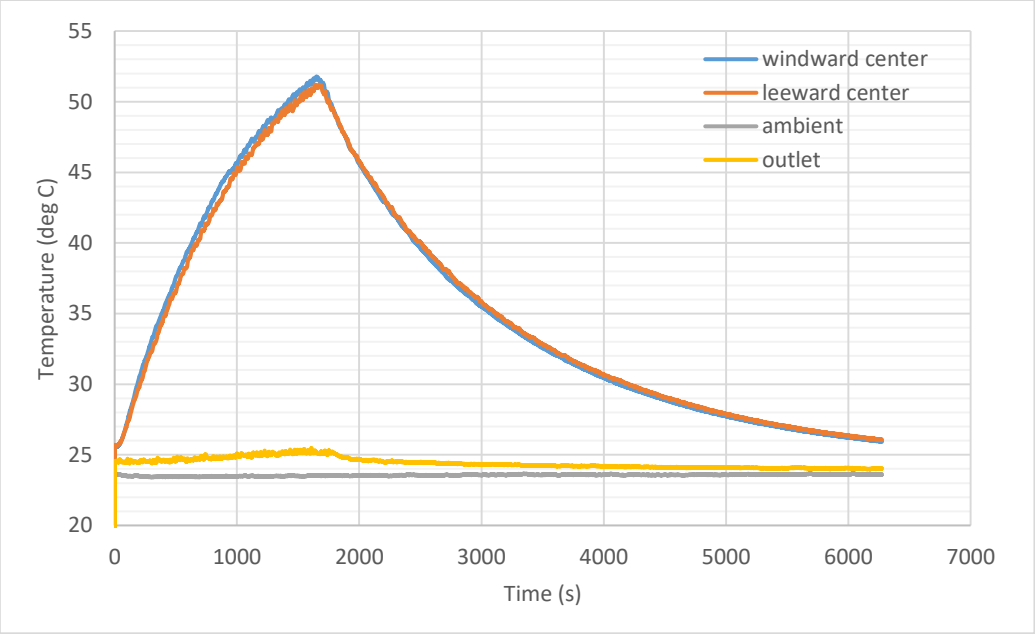

Figure A.1: Temperatures measured at the battery windward, battery leeward, battery pack outlet, and ambient room.

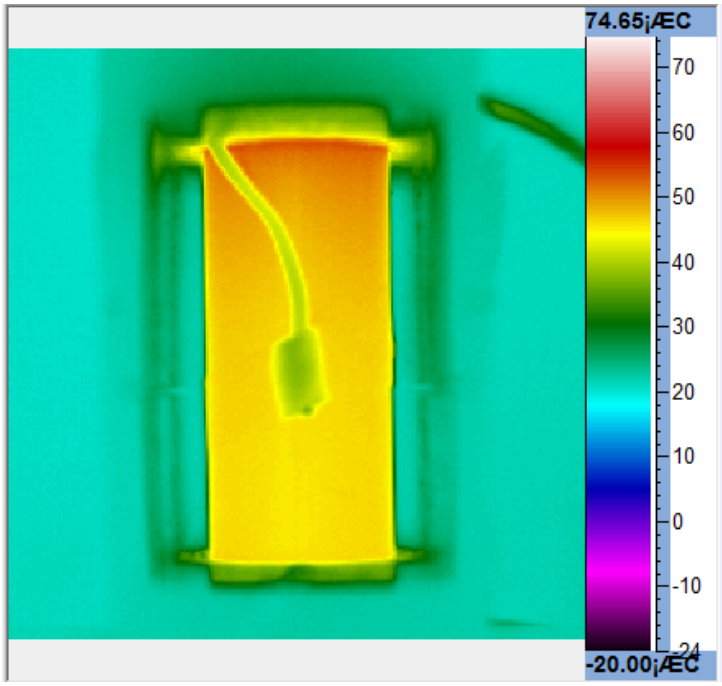

Figure A.2: Temperature contour taken by the thermal camera at 27'30" of discharging.

Appendix B: Comparison of cell-level average surface temperature including chilling period

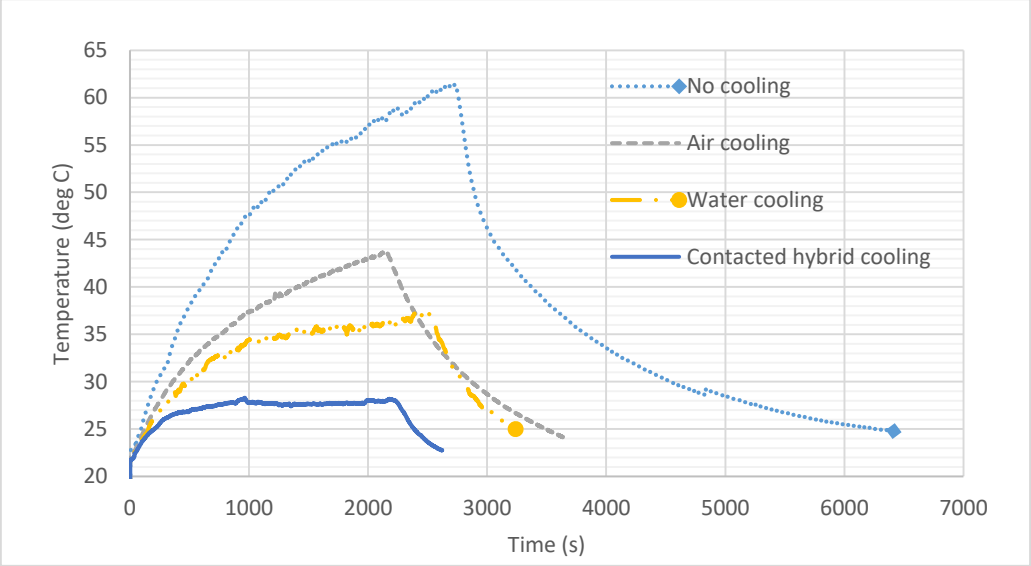

Figure B.1: Temperature trends of different cooling methods during the entire discharging and chilling period.

Appendix C: Temperature non-uniformity of cell-level water-cooling and contacted hybrid cooling test with thermocouple interference

The T-type thermocouple was used in both the water-cooling and the contacted hybrid cooling tests to verify the temperature measured by the thermal camera. To do this, the thermocouple was installed between the coiled fiber channel and the battery surface. This added interferences to the cooling performance, since part of the battery surface was not in contact and properly cooled by the fiber channels. From Figures C.1 and C.2, it can be observed that the temperature non-uniformity is higher than what has been presented in this thesis by about 1 ℃. However, the non-uniformity in the hybrid cooling test remained unchanged after the first linear trend which matches the result presented in this thesis.

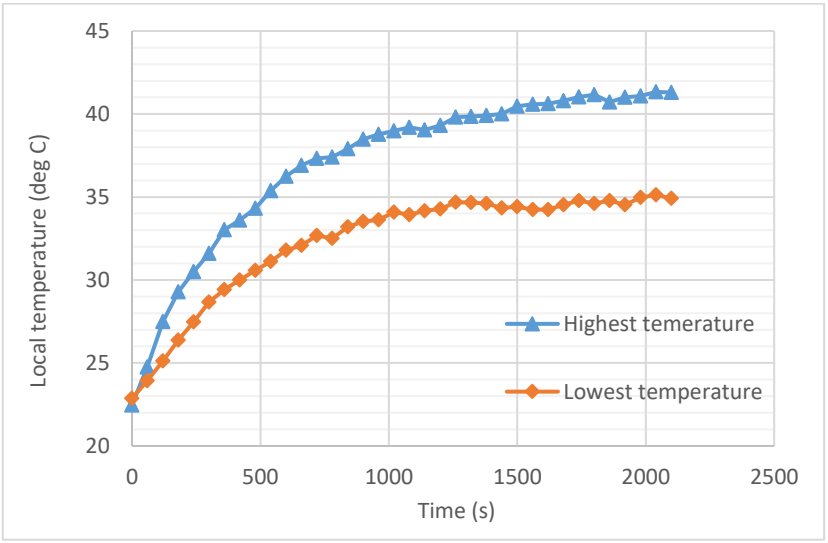

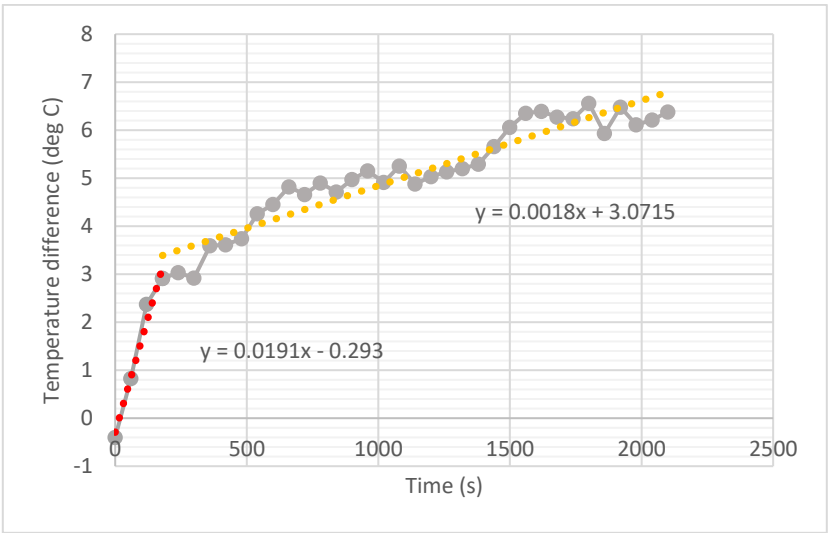

Figure C.1: Local temperatuere (top) and temperature non-uniformity (bottom) of cell-level water-cooling with thermocouple interference

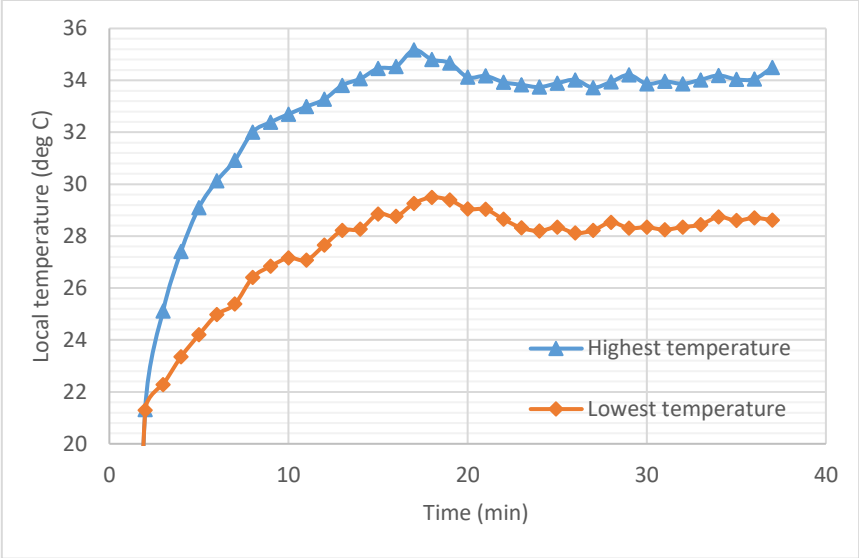

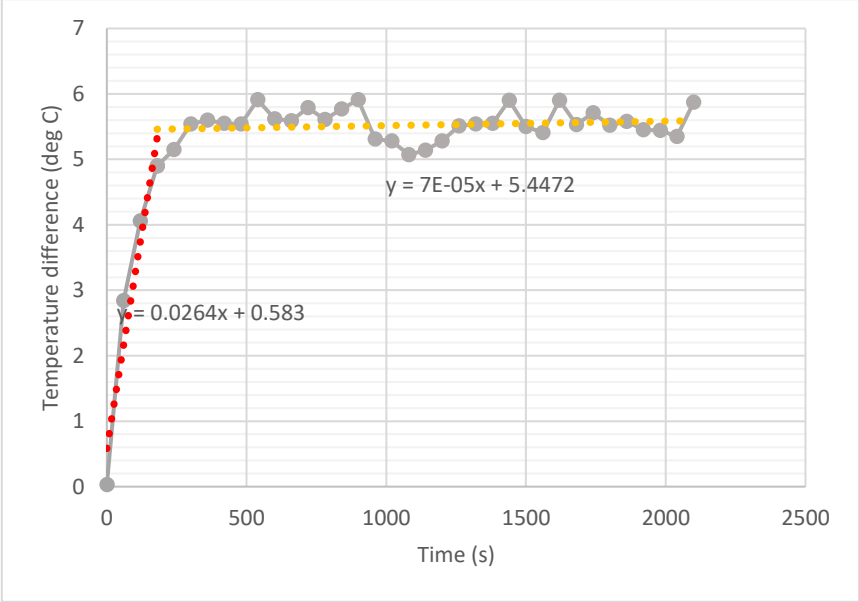

Figure C.2: Local temperature (top) and temperature non-uniformity (bottom) of cell-level contacted hybrid cooling with thermocouple interference